Remote Sensing of Environment 342 (2026) 115461

Contents lists available at ScienceDirect

Remote Sensing of Environment

journal homepage: www.elsevier.com/locate/rse

Near-real-time mapping for causal agents of forest disturbances in China using harmonized Landsat and Sentinel-2 dataset

Ronghua Liao [a,b], Chengcheng Guo [b], Lingkun Chen [a,b], Yulin Jiang [a,b], Yuchen Tao [a,b], Jiani Liao [a,b], Rui Lu [a,b], Huaguo Huang [c], Zhou Shi [a,b], Su Ye [a,b,*]

[a] State Key Laboratory of Soil Pollution Control and Safety, Zhejiang University, Hangzhou 310058, China
[b] Zhejiang Key Laboratory of Agricultural Remote Sensing and Information Technology, Zhejiang University, Hangzhou 310058, China
[c] State Forestry and Grassland Administration Key Laboratory of Forest Resources and Environmental Management, Beijing Forestry University, Beijing 100083, China

ARTICLE INFO

Edited by Marie Weiss

Keywords:
Forest disturbance
Near-real-time
Disturbance agent
Time-series
Latency

ABSTRACT

Timely identification of forest disturbance agents is essential for effective ecosystem management and rapid response to natural and anthropogenic threats. However, most near-real-time (NRT) monitoring systems focus solely on detecting disturbance locations and timing of generic disturbances, lacking attribution of causal agents that is critical for operational decision making. This study presents a novel NRT framework to map major forest disturbance agents—wildfire, logging, and stress—across China using the Harmonized Landsat and Sentinel-2 (HLS) dataset. To address the scarcity of local training data, we introduced a transferring-guided sampling strategy that efficiently generated tile-specific local samples by leveraging disturbance archives from the conterminous United States and subsequent expert verification. Stage-based random forest models were subsequently constructed using 16 temporally dynamic features derived from HLS spectral trajectories to classify anomalies at varying disturbance stages. The system achieved an overall first-alert lag of 11.6 days and a level-off lag of 15.5 days, with corresponding overall accuracies of 77.5% and 84.0%. Wildfire disturbances exhibited the shortest detection lag and the highest accuracy, followed by logging and stress, reflecting differences in spectral separability among agents. Compared with the global DIST-ALERT product, the proposed framework achieved higher accuracy and fewer false detections, at a trade-off of a 3.7-day longer first-alert lag, while providing actionable information on disturbance causality. These results demonstrate the feasibility of operationally mapping disturbance agents in near real-time at a national scale. The proposed framework offers a transferable, data-efficient solution for rapid forest disturbance attribution and provides a foundation for global-scale NRT disturbance monitoring initiatives.

1. Introduction

Driven by climate change and anthropogenic factors, a growing number of forest disturbances from wildfires, logging and insect outbreaks have emerged globally in recent years (Cohen et al., 2016; Seidl et al., 2014; Tyukavina et al., 2017). With increasing frequency and severity, the disturbance events disrupt forest structure and composition, causing severe ecological and economic consequences (Dee et al., 2025; Thom and Seidl, 2016). Only with timely and detailed disturbance maps can forest managers implement mitigation against natural disasters (e.g., wildfire) through rapid damage assessment and evacuation planning (Oddo and Bolten, 2019), or enact actions against illegal and unsustainable forest harvesting (Hansen et al., 2016; Wheeler et al., 2014).

As of 2020, China's forest area reached approximately 220 million hectares, making up about 5% of the world's total forest cover (Sarre, 2020). Given China's large forested areas and rapid economic expansion, effective monitoring helps address forest fragmentation, habitat destruction, and other ecological challenges. Globally exacerbated climate warming also intensifies natural disturbances in China, such as wildfires (Wu et al., 2019; Zhang et al., 2023) and pest outbreaks (Xu et al., 2023). Particularly, China hosts the world's largest planted forest area (Cheng et al., 2024), and these planted forests might be more vulnerable to climate-induced disturbance due to their lower species richness and greater structural homogeneity (Zhong et al., 2021), necessitating timely alerting and intervention.

* Corresponding author at: State Key Laboratory of Soil Pollution Control and Safety, Zhejiang University, Hangzhou 310058, China.
E-mail address: su.ye@zju.edu.cn (S. Ye).

https://doi.org/10.1016/j.rse.2026.115461
Received 23 October 2025; Received in revised form 7 April 2026; Accepted 26 April 2026
Available online 6 May 2026

Near-real-time (NRT) disturbance monitoring refers to performing a disturbance mapping task with minimal delay between remotely sensed image acquisition and decision making. The reported delay ranges from several days (Tang et al., 2023; Ye et al., 2024) to two/three months (Bullock et al., 2022; Reiche et al., 2018; Tang et al., 2019), depending on the temporal resolution of the datasets and the chosen algorithm. The earlier NRT disturbance-related studies focused on coarse-resolution datasets (> 30 m) with high temporal frequency, such as the MODIS products (Reymondin et al., 2012; Verbesselt et al., 2012). Methods such as BFAST Monitor (Verbesselt et al., 2012) and the Terra-I system (Reymondin et al., 2012) have been widely applied to MODIS daily observations to provide rapid disturbance alerts at global or continental scales. With the open-access policy for Landsat (Woodcock et al., 2008), the NRT monitoring was subsequently extended to the medium-resolution dataset (10–30 m) using such as Landsat (Hansen et al., 2016; Pasquarella et al., 2017), enabling more detailed mapping of forest change. Recently, the combination of several satellite platforms, such as Harmonized Landsat and Sentinel (HLS) dataset (Hansen, 2024; Shang et al., 2022), has proven successful in reducing detection lags owing to the enhanced data density. While traditional NRT methods identified spectral anomalies from time-series datasets using a pre-defined threshold for change magnitudes (Olsson et al., 2016; Pasquarella et al., 2017; Shang et al., 2022; Tang et al., 2019; Verbesselt et al., 2012; Ye et al., 2021a), Ye et al. (2024) showed that the retrospective analysis on early signals of historical disturbances through machine learning could considerably improve the timeliness for alerting disturbances in an NRT manner. Despite various datasets and algorithms, almost all existing NRT studies only targeted mapping locations and timing of generic forest disturbances, some of which additionally provided disturbance probability map (Hansen et al., 2016). In a practical monitoring project, knowing why the disturbance occurs in a timely manner is equally important as being informed of where and when, because information on causal agents (e.g., wildfire, logging) is prerequisite for alert prioritization, actionable management and impact assessment (Slagter et al., 2023; Stahl et al., 2023). For example, Andela et al. (2022) showcased separating wildfire disturbances from logging and drought in Amazon holds great importance for wildfire suppression and air quality evaluation for this region. Particularly, given the increasing prevalence of forest disturbances globally, there is a clear need for broadly applicable approaches that can map disturbance causal agents in a timely manner.

The current challenges surrounding NRT disturbance agent mapping are primarily two-fold: methodological limitations and data constraints. While numerous successful studies have mapped historical disturbance agents (Hermosilla et al., 2015; Kennedy et al., 2015; Qiu et al., 2025; Stahl et al., 2023), the retrospective approaches may not be directly applicable or could perform poorly in an NRT task. Most studies have utilized temporal segmentation on annual time series and then classified spectral breaks based upon spectral attributes of the breaks (Hermosilla et al., 2016; Hermosilla et al., 2015; Kennedy et al., 2015; Schroeder et al., 2017; Shimizu et al., 2017). A more advanced approach involved applying an end-to-end deep learning model on annual composite (Chen et al., 2021; Perbet et al., 2024), instead of a two-step procedure for temporal segmentation and break classification. Both approaches generated agent maps annually at their fastest update rate, making them insufficiently timely for an NRT monitoring task. Other approaches chose dense time series as inputs from single-sensor or multi-sensor combination, often processing a long temporal window for post-disturbance observations. As a result, while the estimated disturbance dates can be close to reference dates, their operational timeliness in an NRT context remains limited when disturbances need to be characterized within days to weeks. Zhang et al. (2022) required a synthetic image from one year after the spectral break as one of machine-learning inputs for classifying for boreal forest agents. Likewise, Qiu et al. (2025) included harmonic coefficients of the post-disturbance segment (at least one year) in their land agent classification model. Since these studies were originally designed for historical disturbance mapping, their performance under a lack of long-term post-disturbance features remains uncertain for the NRT scenario. To our knowledge, Slagter et al. (2023) is the only study for addressing disturbance agent mapping in an NRT scenario. Slagter et al. (2023) tested Convolutional Neural Network (CNN) on Sentinel-1 and Sentinel-2 data composited over a period ranging from 1 to 6 months after the disturbance for mapping the driver for small-scale tropical forest disturbances (e.g., road development, selective logging, and mining), reporting that the F_1 score increased along with the increasing post-disturbance period for compositing (1 month: 0.785; 6 months: 0.851). However, this approach suffers two primary limitations when being operationalized for elsewhere in the world: 1) at least one month of detection latency due to its contingency on cloud-free monthly composite; 2) incapability of monitoring deciduous forest disturbances because it ignores the confusion between disturbance signals and seasonal defoliation.

An NRT monitoring of disturbance agents could be further constrained by training data availability. A well-trained machine learning model, built on a sufficient number of high-quality training datasets, not only ensures accurate mapping of disturbance agents but also improves the timeliness of detecting disturbance signals from various spectral anomalies (Ye et al., 2024). Some existing studies manually interpreted a set of disturbance agent samples and established a single classification model that is applied into the study area (Hermosilla et al., 2015; Kennedy et al., 2015; Shimizu et al., 2017; Slagter et al., 2023), while the performance might be compromised if the samples were not optimal for a local region. To fulfill a localized training sampling, historical disturbance dataset have been utilized to automate agent sample labeling in United States (Pastick et al., 2019; Qiu et al., 2025) and in Canada (Zhang et al., 2022), taking advantage of the abundance of public disturbance products in these two countries. This approach enables the use of a local model built for a specific region, ultimately enhancing map quality (Qiu et al., 2025). However, historical disturbance dataset covering comprehensive agents is often unavailable for most regions worldwide, including China. To our knowledge, OPERA Land Surface Disturbance Product (Hansen, 2024) is the only global general disturbance dataset covering China's forest. The OPERA product detects recent spectral anomalies for indicating forest loss but lacks information on disturbance agents.

This study aims to develop a new NRT approach for mapping disturbance agents, with an application to monitoring forest disturbances in China and potential transferability to other regions globally. To overcome the limitation of scarce local training data, we designed a labor-saving workflow to generate local samples at a per-tile basis through a transfer mapping using disturbance samples from CONUS and manual verification. Rich spectral-temporal features following disturbances were extracted from the Harmonized Landsat and Sentinel-2 (HLS) dataset, which provides the densest moderate-resolution observations to date. To enhance discrimination among disturbance agents, particularly during the early stages of disturbance, we constructed stage-specific models informed by the number of consecutive anomalies detected, and applied them for the NRT monitoring scenario. Consistent with previous studies (Hermosilla et al., 2015; Zhang et al., 2022), we adopted a three-agent classification system, consisting of wildfire, logging, and stress, with detailed definitions provided in Table 1.

Table 1
Definition for three major disturbance agents in this study.

Agents	Description
Wildfire	Wildfire in forests or wooded land, including unplanned and prescribed fires
Logging	The removal of forested vegetation by human activity such as timber harvesting and construction, such as clear cutting, selective logging, etc.
Stress	Biological or environmental press that undermines forest health, vigor, or resilience without causing stand-replacing canopy damage, such as insect infestation and drought.

2. Study sites and datasets

2.1. Study sites

We chose the five study sites across a large geography of China, representing a variety of forest types and disturbance agent patterns (Fig. 1). Daxing'anling ("DX"), one of China's most wildfire-prone forest areas, is located in the northwestern Heilongjiang and northeastern Inner Mongolia Province, which is cold-temperate deciduous coniferous forest dominated by *Larix gemelini*. The wildfire for this region mainly occurred in spring and fall, mainly caused by lightning (Zhao et al., 2020). It has been reported that frequency and severity of the lightning-induced wildfires are both increasing recently (Hu and Zhou, 2014). The Sichuan Basin (SB) site, situated in southwestern China, is characterized by evergreen broadleaf forests, mixed conifer–broadleaf stands, and extensive bamboo forests. These ecosystems often contain dense understory vegetation and substantial fuel loads. The accumulation of dry branches, fallen leaves, and intertwined weeds further increases wildfire risk, making the region highly prone to wildfires. The Xiangzhong Basin (XB), situated in central Hunan Province, falls within the subtropical monsoon climate zone, characterized by warm, humid conditions and abundant rainfall. Forest disturbances in this region are primarily driven by logging and wildfire (Cao et al., 2025). In particular, timber harvesting and land conversion were largely driven by wood demand and agricultural expansion, which follows patterns consistent with those observed in other subtropical regions of China. The Yangtze Plain (YP) site, located in Zhejiang Province, is dominated by subtropical evergreen broad-leaved forests and mixed deciduous–evergreen communities, which together sustain a rich diversity of tree species. As one of China's most developed regions, YP contains forests that are highly susceptible to human disturbances, particularly land-use conversion. The last study site, YunNan plateau (YN), hosts diverse forest ecosystems, ranging from tropical monsoon rainforest in the south to evergreen broadleaf forests in higher elevations. According to the past study (Lin et al., 2021), pine shoot beetles have caused extensive tree mortality, leading to considerable ecological impacts across the forests of this region. All sites include all three disturbance agents, with a summary of forest types and primary disturbance agents provided in Table 2.

2.2. Datasets

We used 2016 China Land Cover Dataset (CLCD) product (Yang and Huang, 2021) to define forest pixel population for NRT monitoring. CLCD, one of the most commonly used land cover products for China, was created by training a random forest with temporal metrics using training samples from the public products, which reports to have an overall accuracy of ~80% (Yang and Huang, 2021).

We selected HLS time series datasets as the primary data source for performing the NRT task in China as well as extracting primary disturbance features in CONUS. To create a seamless surface reflectance from

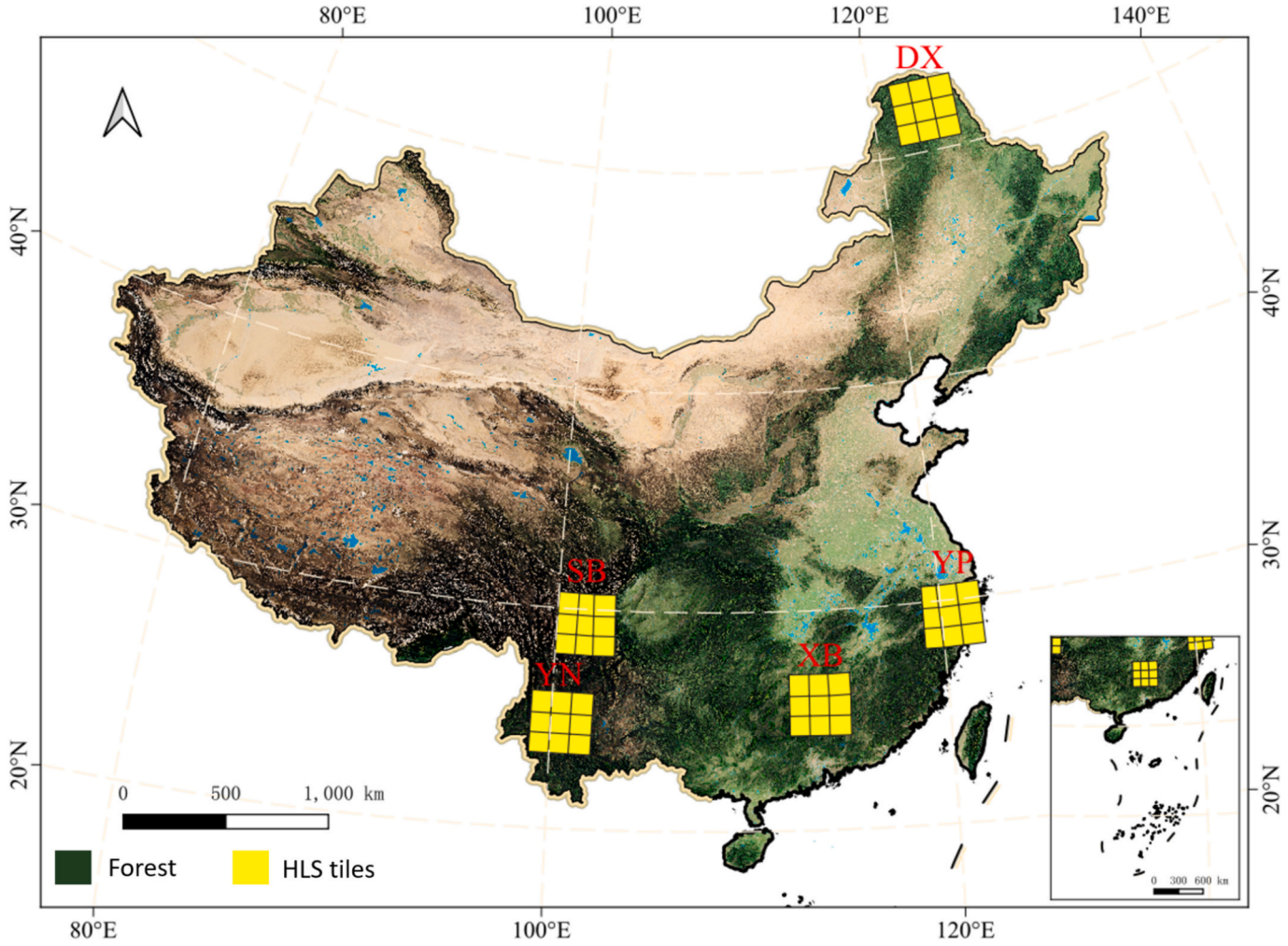

Fig. 1. Five study sites for testing an NRT forest disturbance monitoring in China. For each site, nine adjacent Harmonized Landsat and Sentinel (HLS) tiles were used for testing the performance of the proposed approach (highlighted as yellow polygons). (For interpretation of the references to colour in this figure legend, the reader is referred to the web version of this article.)

Table 2
The forest, disturbance, and datasets for five study sites.

Site name	Primary forest types	Primary tree species	Primary disturbance agents	Selected Harmonized Landsat and Sentinel (HLS) Tiles
Daxing'anling (DX)	Cold-temperate deciduous coniferous forest	*Larix gemelini, Pinus sylvestris, Betula platyphylla*	Wildfires , commerciallogging	51UVU, 51UXU, 51UVT, 51UWT, 51UXT, 51UVS, 51UWS, 51UXS, 51UWU
Sichuan Basin (SB)	Subtropical evergreen broad-leaved forests	*Cyclobalanopsis, Castanopsis, Lithocarpus*	Wildfires	47RPP, 47RQP, 47RPN, 47RQN, 47RPM, 47RQM, 48RTT, 48RTS, 48RTU
Xiangzhong Basin (XB)	Subtropical evergreen broad-leaved forests	*Castanopsis, Cyclobalanopsis, Lithocarpus*	Clear cutting driven by land conversion	49RFJ, 49RGJ, 49RFH, 49RGH, 49RHH, 49RGK, 49RFK, 49RHJ, 50RKQ
Yangtze Plain (YP)	Subtropical evergreen broad-leaved forests, bamboo forests	*Schima superba, Cunninghamia lanceolata, Phyllostachys edulis*	Clear cutting driven by land conversion	50RQU, 50RQS, 50RQT, 51RTP, 51RUP, 51RTN, 51RUN,51RTM, 51RUM
YunNan plateau (YN)	Subtropical evergreen broad-leaved forests, tropical monsoon rain forests	*Pinus yunnanensis, Dipterocarpus turbinatus*	Insect disturbances, wildfire	47RNJ, 47RPJ, 47RQJ, 47RNH, 47RPH, 47RQH, 47QNG, 47QPG, 47QQG

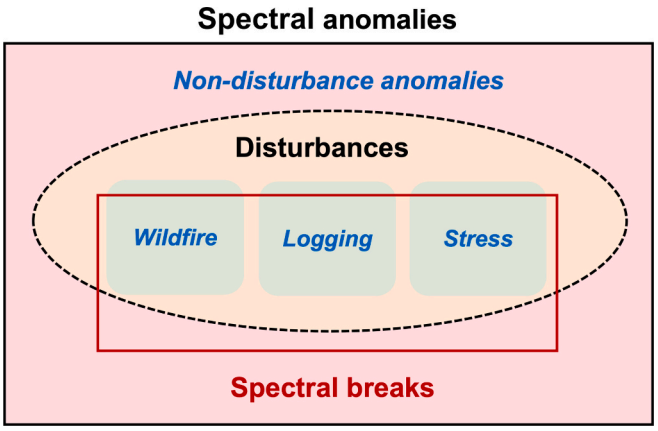

Fig. 2. Spectral anomalies constitute a broad category encompassing all irregular signals detected in satellite-based time-series datasets. A subset of these anomalies emerges as spectral breaks, which represent pronounced and persistent structural shifts in the spectral trajectory. While many spectral breaks are typically associated with forest disturbance events such as wildfire or logging, non-disturbance processes, including vegetation succession and climate variability, can also produce break-like signals. Conversely, certain disturbance events, such as drought stress or understory wildfires, may induce only subtle or short-lived anomalies that do not evolve into detectable breaks. This study aimed to detect and classify spectral anomalies into four categories (blue fonts in the figure): wildfire, logging, stress, and non-disturbance anomalies. (For interpretation of the references to colour in this figure legend, the reader is referred to the web version of this article.)

the Operational Land Imager (OLI) and Multi-Spectral Instrument (MSI) aboard Landsat-8/9 and Sentinel-2 A/B satellites, the HLS dataset harmonizes their products through radiometric calibration, common gridding, bandpass alignment, and geometric co-registration (Claverie et al., 2018; Ju et al., 2025). With four sensors currently in the virtual constellation, HLS provides observations once every 2–3 days with 30-m resolution, offering the highest temporal resolution available for moderate-resolution datasets. To guarantee the densest time series, we hereafter focused on only six spectral bands present on both HLS Landsat (L30) and Sentinel-2 (S30) products (Table S1 of the supplementary material).

Similar to the previous work (Ye et al., 2024), we collected an ensemble of annual CONUS-wide disturbance products from 2017 to 2021, which were used to build the CONUS sample archive for preliminary mapping in China. These products include Landsat-based Burned Area (BA) Science Product (Hawbaker et al., 2020) for wildfire, and Aerial Detection Survey (ADS) insect activity dataset (Johnson and Wittwer, 2008) for stress disturbances. We also include Land Change Monitoring, Assessment, and Projection (LCMAP) Primary Land Cover maps (Xian et al., 2022) and LANDFIRE Annual Disturbance Products (Ryan and Opperman, 2013) to indicate logging regions (see Section 3.1).

3. Methodology

In this study, we adopted a two-level hierarchical framework to define discontinuities detected in the time series: anomaly and break levels. Their relationships with disturbance agents are illustrated in Fig. 2. *Spectral anomaly* refers to any observation where the spectral reflectance deviates from the expected patterns predicted by the historical time series. Such anomalies are not always linked to disturbances; they may instead arise from processes such as succession, phenological shifts, climate variability, or even data noise (Zhu et al., 2022). We therefore categorized those anomalies not directly linked to disturbances as “non-disturbance anomalies”. A “spectral break”, on the other hand, represents a cluster of anomalies with large magnitudes and extended durations, resulting in a structural change in the time series.

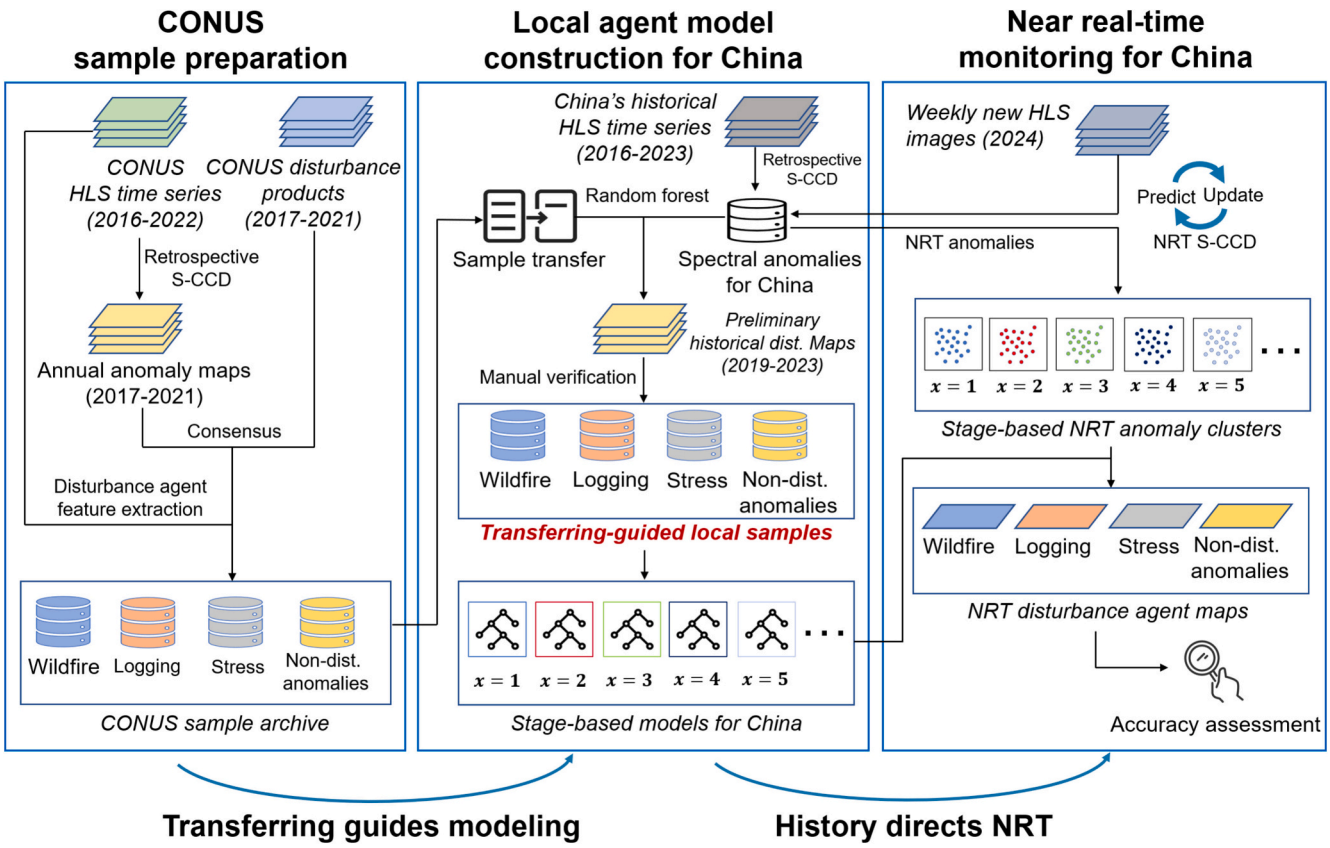

Fig. 3. The three-step workflow of the NRT forest disturbance agent mapping for this study.

Breaks are characterized by significant changes in statistical properties (e.g., mean, variance) between pre- and post-change segments. When a spectral break is detected, the time series model requires re-initialization using a CCDC-like approach, which necessitates at least 12 clear observations and a time span of one year (Zhu et al., 2022). This re-initialization complicates NRT monitoring, as the absence of a stable model in the new segment reduces temporal continuity, therefore a stricter threshold is expected for break detection to minimize unnecessary model reset. To address this challenge, we implemented a unified monitoring workflow with two detection levels following the previous study (Ye et al., 2024): (1) the anomaly level, using a sensitive configuration ($change_{threshold} = 0.90, conse = 3$) to inclusively detect all types of spectral anomalies without triggering model re-initialization; and (2) the break level, using a conservative configuration ($change_{threshold} = 0.9999, conse = 8$) to identify pronounced structural changes that justify model reset. Here, *change_threshold* indicates the chi-square probability for identifying spectral anomalies, while *conse* specifies the minimum consecutive number of anomalies required to confirm a break. Using this conservative break configuration, only 1.7% of forest pixels triggered a break by the final weekly update (Table S2), indicating that model resets were rare. The primary objective of this study is to classify spectral anomalies, rather than breaks, into disturbance agents in an NRT manner.

Our workflow proceeds in three stages (Fig. 3). First, we generated high-quality disturbance agent samples for CONUS by using the consensus between break detection and multiple disturbance products. Next, the CONUS disturbance samples will be used to guide the local sample selection and model construction for China. Finally, these disturbance agent models, built from the local disturbance history, were applied to direct NRT monitoring for recent disturbances.

3.1. CONUS sample preparation

3.1.1. CONUS sample selection

We created a high-confidence agent sample archive from the consensus between spectral anomaly detection and CONUS-wide disturbance products. Fifty HLS grids were randomly sampled across CONUS (Fig. S1 in the supplementary), covering a variety of geographic extent. The Stochastic Continuous Change Detection (S-CCD) algorithm (Ye et al., 2021a) was implemented on all available HLS images of each tile (2016–2022) and produced a series of annual spectral anomaly maps from 2017 to 2021. S-CCD (https://github.com/Remote-Sensing-of-Land-Resource-Lab/pyxccd), a short-memory adaptation of the CCDC algorithm that incorporates the Kalman filter, has two functionalities for this study: retrospective analysis for historical anomalies and NRT monitoring for the most recent anomalies. This approach ensures the consistent feature generation between the retrospective and the NRT scenario. The anomalies for the first (2016) and the last year (2022) of data range were excluded because the quality of spectral anomalies are often unsatisfactory for CCDC-like algorithms.

For open-access disturbance products, we first generated a general disturbance map at an annual step by combining Landsat-based BA product, ADS dataset for stress samples, the category transition map from differencing LCMAP Primary Land Cover maps between two neighbor years, and the annual LANDFIRE disturbance map. By overlapping the general disturbance map with its corresponding annual spectral anomaly map, we identified four distinct sample pools: one for wildfire disturbances, defined by spectral anomalies within the Burned Area (BA) region; one for stress disturbances, linked to spectral anomalies overlapping the insect-impact region as indicated by the ADS map; one for logging disturbances, consisting of spectral anomaly pixels within forest transition regions identified by category changes in LCMAP

cover maps or marked as "logging" in the LANDFIRE disturbance map; and one for non-disturbance anomalies (e.g., phenological shifts, image noises), which are those spectral anomaly pixels outside the extent of general disturbances. We applied stratified sampling to collect 2000 samples from each sample pool per HLS tile for each year (2017 to 2021). For 50 CONUS tiles, we reached the final CONUS sample archive, consisting of four PIXEL pools, i.e., logging ($n = 356{,}604$), wildfire ($n = 310{,}500$), stress ($n = 76{,}500$) and non-disturbance anomaly pool ($n = 386{,}594$), after excluding non-forest pixels.

3.1.2. Disturbance agent feature extraction

We extracted 16 disturbance agent features for CONUS samples, comprising three pre-disturbance features, nine trajectory-based change features, two general change features, one disturbance-date feature and one data-density feature. Like other CCDC-type algorithms, S-CCD produces temporal features (e.g., harmonic coefficients and break-based change magnitudes) for each original band. Accordingly, the predicted reflectance $\widehat{\rho}_{i,x}$ for xth observation since the first anomaly signal at the ith HLS band ($i = 1, 2, \ldots, 6$) is reconstructed from the pre-disturbance harmonic coefficients:

$$\widehat{\rho}_{i,x} = a_{0,i} + \sum_{k=1}^{n=2}\left(a_{k,i}\cos\left(\frac{2\pi k}{T}date(x)\right) + b_{k,i}\cos\left(\frac{2\pi k}{T}date(x)\right)\right) + c_{1,i}date(x) \quad (1)$$

Where $a_{k,i}$ and $b_{k,i}$ are the harmonic coefficients, k is temporal frequency of harmonic component, n is the number of harmonic pairs (note that n=2 for S-CCD), T is the number of days per year (T=365.25). Following Zhang et al. (2022), we reduced the six HLS spectral bands into three physically meaningful components, namely brightness, greenness, and wetness, using the Tasseled-Cap (TC) transformation. This feature reduction effectively halved the dimensionality of the input space, thereby alleviating potential overfitting and poor generalization associated with a high-dimensional feature input (Verleysen and François, 2005). The three pre-disturbance features, selected for disturbance agent prediction in this study, were derived from the predicted reflectance at the first post-anomaly observation ($x = 1$):

$$\begin{bmatrix}\widehat{\rho}_{bri,pre}\\ \widehat{\rho}_{gre,pre}\\ \widehat{\rho}_{wet,pre}\end{bmatrix} = B \bullet \begin{bmatrix}\widehat{\rho}_{1,1}\\ \widehat{\rho}_{2,1}\\ \widehat{\rho}_{3,1}\\ \widehat{\rho}_{4,1}\\ \widehat{\rho}_{5,1}\\ \widehat{\rho}_{6,1}\end{bmatrix} \quad (2)$$

The matrix B represents the TC coefficient matrix for Landsat 8, as outlined in (Baig et al., 2014). Since the Sentinel-2 data in the HLS dataset was "spectrally adjusted to match Landsat 8/OLI spectral bandpasses" (Claverie et al., 2018), it is appropriate to use the Landsat 8 TC coefficients for HLS. The coefficients are as follows:

$$B = \begin{bmatrix} 0.3037 & 0.2793 & 0.4743 & 0.5585 & 0.5082 & 0.1863 \\ -0.2941 & -0.243 & -0.5424 & 0.7276 & 0.0713 & -0.1608 \\ 0.1511 & 0.1973 & 0.3279 & 0.3406 & -0.7117 & -0.4559 \end{bmatrix} \quad (3)$$

In addition, S-CCD preserves the eight multispectral observations since the first anomaly observation signal. This enables the calculation of each band-specific change magnitude at the xth post-anomaly observation ($x = 1, 2, \ldots, 8$) for the ith band ($i = 1, 2, \ldots, 6$):

$$CM_{i,x} = \widehat{\rho}_{i,x} - \rho_{i,x} \quad (4)$$

Where $\rho_{i,x}$ and $\widehat{\rho}_{i,x}$ represents the actual and predicted reflectance for xth observation since the first anomaly signal at the ith band. Correspondingly, the TC-based change magnitudes were derived as linear combinations of these band-wise change magnitude:

$$\begin{bmatrix}CM_{bri,x}\\ CM_{gre,x}\\ CM_{wet,x}\end{bmatrix} = B \bullet \begin{bmatrix}CM_{1,x}\\ CM_{2,x}\\ CM_{3,x}\\ CM_{4,x}\\ CM_{5,x}\\ CM_{6,x}\end{bmatrix} \quad (5)$$

We further constructed spectral trajectories by tracking $\rho_{bri,x}$, $\rho_{gr,x}$, and $\rho_{wet,x}$ across successive post-anomaly observations ($x = 1, 2, \ldots, 8$). From each trajectory, a set of descriptors was derived in the two-dimensional feature space (*date*, ρ). Specifically, *Slope* denotes Theil-Sen slope representing the general spectral trend after disturbance occurrence. *Intercept* is the intersecting point between the first anomaly date and the Theil-Sen trendline, which represents the initial post-anomaly feature value. Because trajectories may deviate from linearity, *skewness* of the residuals is used to quantify asymmetric departures from the fitted linear trend:

$$skewness_x = \frac{1}{x}\sum_{i}^{x}\left(\frac{e_i - \overline{e}}{s}\right)^3 \quad (6)$$

Where x is the current number of successive anomalies since the first anomaly signal, e_i is the residual between the predicted $\widehat{CM_i}$ by the Theil-Sen linear equation and the actual CM_i, and s is the standard deviation of e_i. As a result, for each anomaly segment, nine trajectory-based features were generated corresponding to three trajectory descriptors (*slope*, *intercept*, and *skewness*) for each of the three TC components (brightness, greenness, and wetness). We assigned zeros to them if x=1. Notably, trajectory-based features could differentiate disturbance agents to some degree (see Fig. S2), but are not assumed to exhibit a universal, globally consistent pattern across all regions. We used these features primarily for local discrimination, as our disturbance-agent classifiers were trained on a per-tile basis using locally verified samples, allowing the models to learn region-specific relationships between trajectory descriptors and disturbance agents.

In addition, we incorporated two general change features from

Table 3
Definition of 16 disturbance agent features for this study. "Time-varying" means that the features are varying with post-anomaly observation collection in an NRT scenario for a pixel.

Predictor name	Description/Equation	Time-varying
1. Pre-disturbance features	$\widehat{\rho}_{bri,pre}$, $\widehat{\rho}_{gre,pre}$, $\widehat{\rho}_{wet,pre}$	No
2. Spectral-trajectory descriptors	$slope_{bri}, slope_{gre}, slope_{wet}$, $intercept_{bri}, intercept_{gre}, intercept_{wet}, skewness_{bri}, skewness_{gre}, skewness_{wet}$	Yes
3. Normalized change magnitude	$CM_{normalized,x} = \sum_{i=2}^{6}\left(\frac{CM_{i,x}}{rmse_{i,x}}\right)^2$	Yes
4. Spectral consistency angle	$angle = \frac{1}{n-1}\sum_{j=1}^{n-1}\beta_{j,j+1}$	Yes
5. First anomaly day of year (DOY)	DOY of the first anomaly observation	No
6. Anomaly span	$ndays = lastobs\_dat - dist\_dat$	Yes

Note: $\beta_{j,j+1}$ is the change-vector angle from jth to $j+1$th anomaly; *lastobs_dat* and *dist_dat* are the last available observation date and the disturbance starting date.

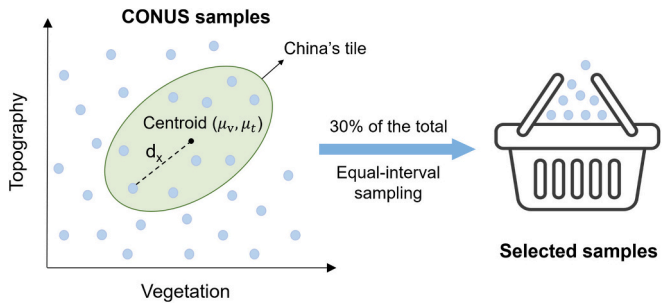

Fig. 4. Conceptual figure for transferring CONUS samples for a specific China's HLS tile. A vegetation–topography feature space is constructed for all CONUS samples. The target domain is defined by the feature distribution of the target tile. After similarity screening (top 30%) and equal interval sampling, a representative sample set matching the target domain is generated for subsequent local model training.

COntinuous monitoring of Land Disturbances (Zhu et al., 2019a, 2019b), i.e., normalized change magnitudes and spectral consistency angle, which has shown effectiveness for distinguishing true disturbances from noisy signals, especially when multiple consecutive anomalies are available. Finally, we added "first anomaly day of year" to account for the occurrence date of a disturbance (e.g., wildfire disturbances occur more in April in China due to tomb-sweeping practices for Qingming Festival), and "anomaly span" to incorporate the effects of data density. Collectively, we adopted 16 disturbance features for building agent classification models (Table 3). Of note is that as a part of disturbance features are time-varying with more observation being collected (see Table 3), we created a set of features for every possible number of consecutive anomalies from ($x = 1, 2, \ldots, 8$).

3.2. Local agent model construction for China

For each targeted HLS tile in China, we first applied retrospective S-CCD to all available HLS images from 2016 to 2023. This process yielded segment-based harmonic coefficients at the per-pixel level, together with 16 disturbance-agent features for all identified anomalies. These outputs served three purposes: (1) characterizing the vegetative conditions of each tile to guide the selection of the most appropriate CONUS subsample; (2) providing spectral anomalies and their associated features for constructing preliminary historical disturbance maps; and (3) supplying the initial data inputs for recursive updates in the NRT monitoring framework. A detailed description is provided below.

3.2.1. Sample transfer

Building upon "similar geographic configurations lead to similar geographic processes" (Zhu et al., 2018), which has been successfully applied in sample transferring (Cui et al., 2025; Hou et al., 2025; Zhu et al., 2019a, 2019b), we proposed the hypothesis that "the more similar the topographic and vegetation conditions, the more similar the disturbance spectral features are". Based on this, we developed a method for selecting a subsample from the CONUS sample archive that most closely matches the characteristics of a targeted HLS tile in China (Fig. 4). The topographic variables considered include the digital elevation model (DEM) and slope, derived from Shuttle Radar Topography Mission (SRTM) data (Yang et al., 2011). The vegetative variables consist of pre-disturbance TC brightness, TC wetness, and TC greenness, which were calculated from synthetic surface reflectance images (dated July 1, 2016) generated through segment-based harmonic coefficients, following the CCDC framework (Zhang et al., 2022; Zhu et al., 2015). Each targeted tile was characterized by constructing a multivariate normal distribution based on these two topographic and the three vegetative variables. Their mean vector (μ) and covariance matrix (S) were computed from the "forest" pixels identified by the CLCD product. Then, we computed Mahalanobis distance between each U.S. sample (k) and the multivariate distribution:

$$d_x = \sqrt{(k-\mu)^T S^{-1} (k-\mu)} \tag{7}$$

We ranked the samples in each of the four CONUS sample pools by their Mahalanobis distance to the targeted China tile and selected the top 30% as the initial sample set. To evaluate this strategy, we compared the average Bhattacharyya distance (BD) between (1) the full CONUS samples and the local China samples (derived from expert-verified preliminary maps; Section 3.2.2), and (2) the selected CONUS samples and the same local China samples, across 45 target tiles. BDs were computed for the four most informative disturbance features, as identified by random-forest Gini importance (Section 3.2.3). The results (Fig. S3 of the supplementary material) show that BDs decreased after selection for stress and wildfire, indicating that the distribution of transferred samples becomes more similar to the target-domain samples when guided by topographic and vegetation similarity. In contrast, BD changes were more variable for logging, likely reflecting greater heterogeneity and region-specific management practices that are not represented during sample transfer. Overall, these results suggest that topographic and vegetative matching can effectively improve cross-region sample alignment, particularly for natural disturbances, thereby strengthening subsequent disturbance mapping.

For the agent proportion, we first used an empirical equation from the previous study to determine the proportion for non-disturbance anomalies (Ye et al., 2024). The proportion was calculated as:

$$Prop_{nodisturb} = 0.9 - (CONSE - x)*0.02 \tag{8}$$

Where CONSE is the maximum number of consecutive anomalies, set to 8, x is the number of consecutive anomalies to be investigated. We used $x = 6$, as six consecutive anomalies has been widely used for CCDC-like approach as the default parameter (Xian et al., 2022; Zhu et al., 2020; Zhu and Woodcock, 2014). Therefore, the proportion for non-disturbance anomalies is 86% (i.e., 0.9 – (8–6) * 0.02). The remaining sample number were equally distributed to three disturbance agents. A total of 10,000 CONUS samples spanning from 2017 to 2021 was applied for each tile, following the previous work (Ye et al., 2024). As a result, the sample numbers for non-disturbance anomalies, wildfire, logging, and stress were 8600, 467, 467, and 467, respectively. Equal prior probabilities were assumed for all disturbance agents, since their relative area proportions could not be estimated prior to the generation of the classification map (Qiu et al., 2025).

From this set, we then applied an equal-interval sampling strategy to construct CONUS samples per sample pool. For instance, within the wildfire pool (310,500 samples), we retained the top 93,150 samples (30%) and subsequently selected every 199th sample (93,150/467) in ascending order of Mahalanobis distance. The equal-interval sampling approach minimizes redundancy from any single geographic region, thereby enhancing the overall diversity of the selected samples.

3.2.2. Transferring-guided local samples

We collected 10,000 CONUS samples from the sample-transfer procedure and transfer 16 disturbance-agent features from CONUS (Table 2) derived from six consecutive anomalies (x = 6) to train an initial random forest model for each tile. These features represent a multi-dimensional feature space that combines both pre-disturbance signatures and disturbance-process changes, improving separability among disturbance agents. We note that we did not explicitly incorporate land management policies or other socio-economic features into the NRT agent classification framework, mainly because adequate high-resolution, spatially consistent socio-economic and policy datasets are not readily available for our study regions. Nevertheless, regional differences in management intensity, land use pressure, accessibility, and enforcement can strongly influence both the frequency and composition of disturbance agents, likely contributing to the spatial variability in

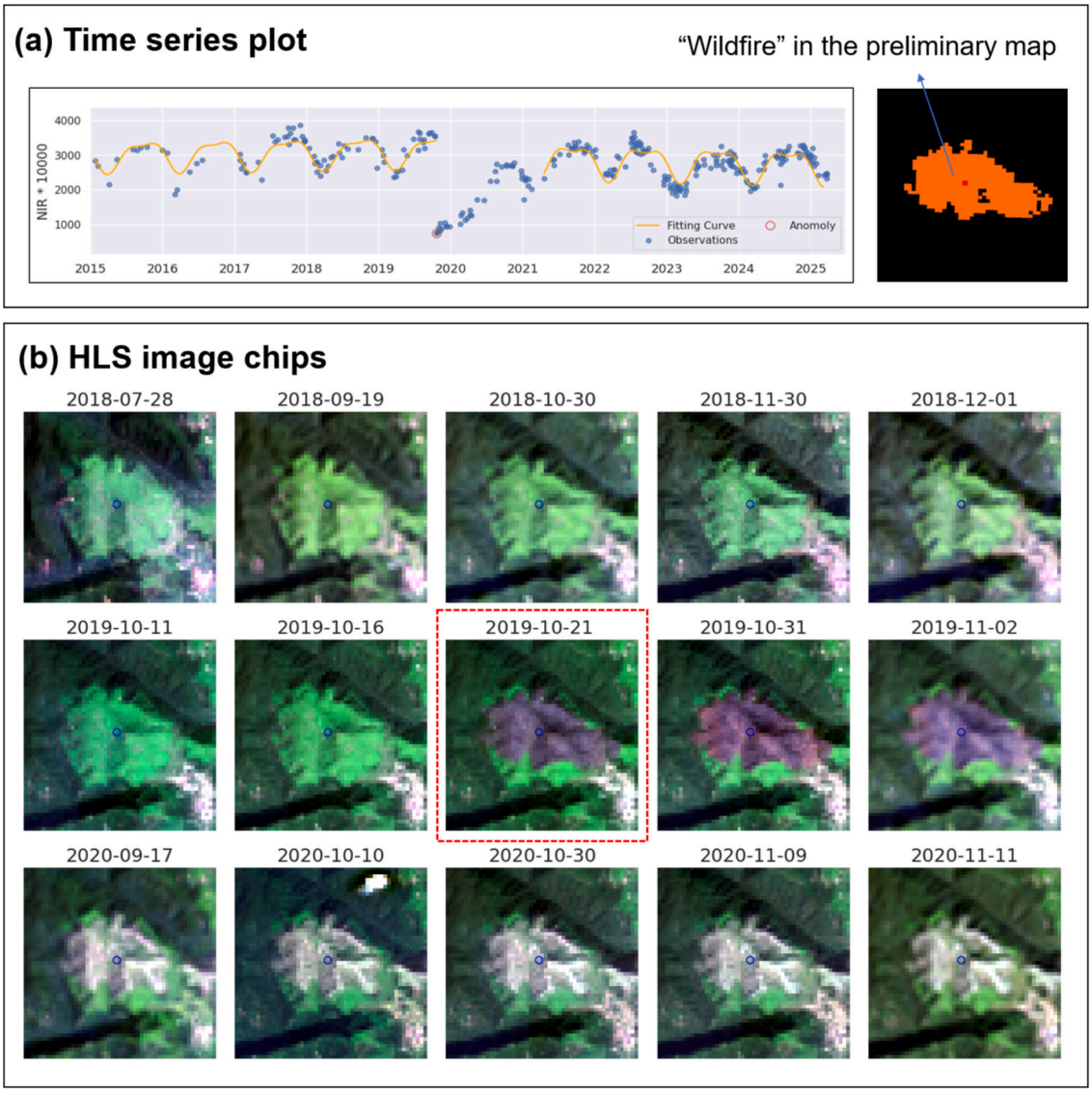

Fig. 5. Manual verification example for a patch labeled as wildfire in the preliminary disturbance mapping (Latitude: 28.1524° N; Longitude:120.1326° E). (a) Time-series trajectory showing a distinct temporal break characterized by a sharp decrease in NIR reflectance. (b) HLS image chips (true colour composite) acquired near the disturbance date across three consecutive years. The observed burn scar and concurrent spectral decline confirmed that the preliminary wildfire label was correctly assigned.

disturbance regimes observed across the five study sites. Accordingly, our workflow was designed to be locally adaptive, because models and class proportions were constructed on a per-tile basis with local verification, which helped accommodate regional differences in disturbance regimes even when the underlying drivers differ.

Subsequently, we applied S-CCD to all available HLS imagery to detect spectral anomalies for each forest pixel in the targeted tiles between 2019 and 2023. The anomalies were then input into the tile-specific random forest model to produce a five-category map: wildfire, logging, stress, non-disturbance anomalies, and anomaly-free forest. The "anomaly-free forest" class includes forested pixels where no spectral anomalies were detected by S-CCD in history, indicating that these areas have not experienced detectable spectral changes in the time period analyzed. For each annual disturbance map, we connected two neighborhood pixels with the same category and generated historical disturbance agent patch maps from 2019 to 2023, which consisted of three types of disturbance agents as well as the non-disturbance anomaly category. Among them, we selected 1000 disturbance agent patches for each of the four categories (wildfire, logging, stress, and non-disturbance anomalies) within each HLS tile, evenly distributed to each year from 2019 to 2023. To address the uncertainties in the preliminary mapping results, four experienced interpreters were recruited to manually verify the patch labels. The verification was based on pre-made figures that included both HLS time-series plot of the center pixel and HLS image chips (see the example of Fig. 5). All interpreters received training and testing prior to the labeling task to ensure consistent interpretation criteria and efficient review. Only patches with high confidence in their assigned labels were retained. To assess the efficiency of this transferring-guided approach, we recorded the time with each interpreter required to complete their respective verification tasks. The verified patches were subsequently dissolved to the pixel level to establish four high-quality local sample pools. The verification outcomes and the corresponding time consumption are summarized in Table S3 of the supplementary material. On average, for each HLS tile, an interpreter required approximately 2.1 h to verify 4000 disturbance patches from the preliminary mapping, of which 1697 patches (~42%) were labeled as high-confidence disturbance agent patches, yielding a total of 38,286 sample pixels (Table S3). This high interpretation

efficiency is partially attributed to the fact that the interpreters were not required to determine the disturbance date, as this information had already been provided by the S-CCD-derived break date.

We set a total of 10,000 final local samples for each HLS tile to construct the final local machine learning model. These samples were drawn from the pixel pool verified to be correct from preliminary mapping. For categorical allocation, the proportion of non-disturbance anomalies was determined as a negative function of the number of consecutive anomalies (x), following Eq. 8. This design increases the relative proportion of disturbance samples when x is small, thereby enhancing detection sensitivity during the early disturbance stage (Ye et al., 2024). The remaining proportion was distributed among disturbance agents according to their relative pixel frequencies verified as correct, ensuring that dominant disturbance types were assigned more samples. The minimum sample number per category is set to 300 pixels, which guarantees that the minority category will not be underrepresented. Accordingly, we prepared eight sets of local samples corresponding to the eight possible numbers of consecutive anomalies ($x = 1, 2, \ldots, 8$) for each tile.

3.2.3. Stage-based local models for China

We constructed stage-based disturbance agent models for each tile using the corresponding sample sets and their 16 agent-based features (Table 3), with the disturbance stage indicated by the number of consecutive anomalies. This stage-wise design allowed us to capture the statistical relationships more acutely between the features and disturbance agents, particularly during the early stage when a disturbance had just begun (i.e., $x = 1$ *or* 2). As such, eight disturbance agent models ($x = 1, 2, \ldots, 8$) were trained from local samples for the NRT mapping. We also assessed the average Gini-based feature importance across all tiles for these eight models (Fig. S4 in the supplementary material). The analysis reveals that (1) normalized change magnitude and spectral consistency angle are consistently the most important features, and (2) spectral-trajectory descriptors, especially the greenness and brightness intercepts, exerts a significant role in influencing the model performance across all stages.

3.3. Near-real-time mapping in China

We implemented NRT disturbance-agent monitoring for 2024 across the five study sites using a weekly updating frequency, which resulted into 52 weekly agent classification maps. In the NRT workflow, each pixel was first evaluated for its current number of consecutive anomalies. This procedure generated eight NRT anomaly clusters, corresponding to disturbance stages ranging from one to eight consecutive anomalies. Each cluster was then classified by its corresponding random forest model into the four categories (logging, wildfire, stress, and non-disturbance anomalies), using 16 disturbance features extracted from the current anomaly segment. The results were aggregated into a weekly NRT disturbance-agent map, based on the spatial locations of the detected anomalies. To mitigate false positives, we applied a filtering rule that excluded “stress” pixels with only one consecutive anomaly, as the weak early-stage signals of stress disturbances are often indistinguishable from phenological variability or data noise. In addition, we grouped adjacent pixels with the same disturbance agent labels into disturbance patches using connected-component labeling and applied a sieving filter to remove small isolated detections. Specifically, patches smaller than 0.3 ha (fewer than four 30 m HLS pixels) were removed to reduce salt-and-pepper noise.

Notably, despite the harmonization efforts in HLS, residual inter-sensor effects (e.g., subtle radiometric inconsistencies and occasional sub-pixel misregistration) may still occur and could potentially trigger spurious anomaly signals. To reduce these impacts, we applied the HLS quality masks and detected anomalies normalized by multi-band residual departures using a chi-square decision rule, which was less sensitive to small sensor-to-sensor biases that tended to manifest as high-frequency noise. In addition, our workflow further suppressed single-date artifacts through temporal persistence (consecutive anomalies and stage-based models), explicit inclusion of a non-disturbance anomaly class during training, and a spatial sieving filter that removes very small isolated patches.

Finally, we developed an NRT platform to implement the weekly updating procedure and to visualize the resulting disturbance-agent maps. The website address is https://forestwatch.com.cn. The interface of this website was displayed in Fig. S5 of the supplementary material.

3.4. Accuracy and latency assessment

We conducted accuracy assessments at the study-site level. For each site, 1200 pixel-based samples were generated using stratified random sampling, with 300 samples assigned to each of the four categories: wildfire, logging, stress, and non-disturbance forest (including non-disturbance anomalies and anomaly-free forest). The four strata were defined as all the pixels being labeled from an ensemble of 52 weekly NRT disturbance agent maps. Across the five representative study sites, this yielded a total of 6000 samples for evaluating the overall model performance. Experienced interpreters manually determined the reference disturbance category and occurrence date for each sample pixel primarily using daily 3-m Planet imagery. Additionally, for stress validation, we relied on the HLS time-series interpretation for (1) a significant SWIR2 increase with stable NIR band (e.g., bark borer) (Ye et al., 2021b) or (2) a pronounced NIR drop followed by rapid recovered (e.g., defoliator) (Silva et al., 2013). The occurrence date was defined as the first day on which an anomaly signal could be visually identified from the Planet image, enabling evaluation of the system's detection latency under operational conditions. Of note is that daily Planet imagery was not guaranteed for all study sites (with approximately 30% of the days missing), which could introduce some uncertainties when interpreting the reference disturbance dates. Despite this limitation, we believe that using Planet imagery remains the most reliable method available for interpreting the reference dates.

We first used these samples to assess individual agent mapping accuracy across 52 weekly NRT agent maps in 2024. Following the sigmoid framework proposed by Bullock et al. (2022), we generated lag-accuracy curves for each agent to illustrate how accuracy varies with detection lag. The lag was defined as the temporal difference between the map production date (i.e., the weekly update date on our NRT platform) and the reference disturbance date interpreted from Planet imagery. For each lag interval, we constructed a confusion matrix and calculated user's accuracy (UA), producer's accuracy (PA), and, F_1 score for each disturbance agent, thereby forming the lag-accuracy curves for inspection. We then will derive two key lags: the first-alert and level-off lags. The first-alert lag, also termed as Mean Time Lag for the First Alert (Reiche et al., 2018), is defined as the average time between the reference disturbance date and the first correct classification by the platform. This metric quantifies the system's responsiveness in issuing its earliest correct alerts, considering only disturbances that were correctly identified (Bullock et al., 2022). The level-off lag (Bullock et al., 2022) will be employed to evaluate the latency and the model performance when the NRT model accuracy plateaus. The level-off lag was determined as the point of maximum vertical distance (y-value) between the curve and a rotated virtual line (45° around the straight line connecting the curve's endpoints).

For the multi-agent assessment, we calculated the overall first-alert and level-off lags as the weighted means across the three disturbance agents, using their total mapped area proportions by aggregating 52 weekly resultant maps as weights. We reported the snapshot-based confusion matrices and Overall Accuracy (OA) at the two overall lag times. Because stratified sampling was employed for the reference data, all accuracy metrics were adjusted by the mapped area proportions, following the recommended best practices outlined by Olofsson et al.

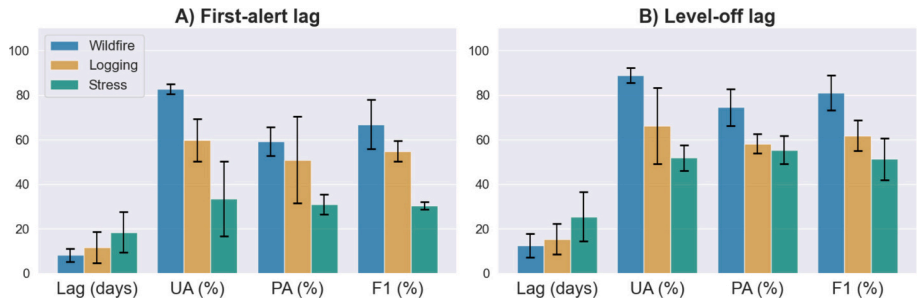

Fig. 6. The average accuracy metrics for three disturbance agents at their first-alert and level-off lags across five study sites.

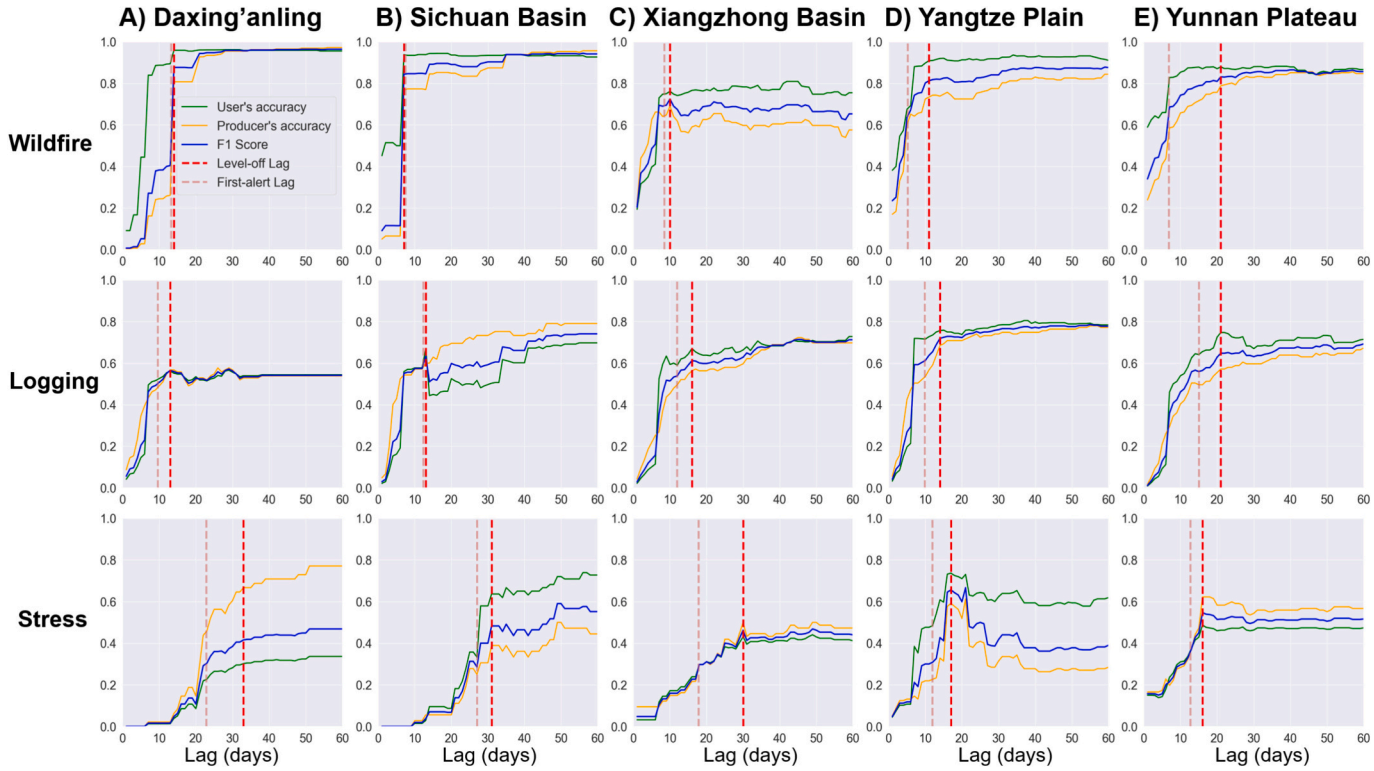

Fig. 7. The lag-accuracy curves for three individual disturbance agents. The first-alert and level-off lags were marked respectively as the light red and dark red dashed line. (For interpretation of the references to color in this figure legend, the reader is referred to the web version of this article.)

(2014). We note that our accuracy assessment targets the end-to-end NRT outputs, and therefore the reported commission and omission errors implicitly include uncertainties from both S-CCD anomaly detection and subsequent agent classification.

For benchmarking, we compared our NRT products with OPERA's DIST-ALERT product (Hansen, 2024), which detects globally reductions in vegetation fraction whenever a new clear observation is acquired. By referencing a historical baseline for the same time of year, DIST-ALERT adjusts for seasonal vegetation dynamics and reduces false alerts. Similar to our platform, DIST-ALERT is based on time-series analysis of the HLS dataset and is updated approximately weekly; however, it only identifies general disturbances without distinguishing among agents. Accordingly, we limited our comparison to binary detection accuracy and latency (i.e., disturbance vs. no disturbance). We reported the comparative lags, UA, PA, F_1, and the level-off OA under the binary scenario (disturbances vs no disturbances), with the latter adjusted by each category's area proportion respectively from the proposed and DIST-ALERT.

4. Results

4.1. Individual disturbance assessments

Fig. 6 shows the variations in the average lags and accuracies over the five study sites across three disturbance agents. The NRT mapping for wildfire disturbances achieved the shortest first-alert lag (8.2 days) and the earliest level-off point (12.6 days) among the three agents, along with the highest UA (82.6%, 88.8%), PA (59.2%, 74.5%), and F_1 scores (0.669, 0.81). This is likely attributable to the strong low-reflectance signal of burn scars shortly after wildfire events, which enables rapid and accurate detection. Logging disturbances exhibited intermediate latency, with the first-alert lag of 11.7 days and the level-off lag of 15.4 days. Stress disturbances required the longest time to be detected, with a first-alert lag of 18.4 days and a level-off lag of 25.4 days. This longer latency can be explained by their more ambiguous spectral feature as well as our definition that a stress pixel must show at least two consecutive anomalies. Stress disturbances also was reported to have the lowest UA (33.6%, 51.9%), PA (33.1%, 55.4%), and F_1 scores (0.305, 0.513) when the two key lags were reached, indicating greater

Table 4
Snapshot-based confusion matrices at the overall first-alert lag (12 days).

Reference					
Map	Wildfire	Logging	Stress	Non-disturb.	Total
Confusion matrix, sample counts					
Wildfire	691	23	3	65	782
Logging	31	305	16	150	502
Stress	8	9	85	295	397
Non-dist. Forest	418	237	318	3346	4319
Total	1148	574	422	3856	6000
Confusion matrix, area proportion adjusted by mapped area proportion (Table S4)					
Wildfire	0.00013	0.00000	0.00000	0.00001	0.00015
Logging	0.00008	0.00083	0.00004	0.00041	0.00136
Stress	0.00000	0.00000	0.00001	0.00004	0.00006
Non-dist. Forest	0.09663	0.05479	0.07351	0.77350	0.99843
Total	0.09685	0.05562	0.07357	0.77397	1.00000
OA	0.00013 + 0.00083 + 0.00001 + 0.77350 = 77.5%				

Table 5
Snapshot-based confusion matrices at the overall level-off lag (16 days).

Reference					
Map	Wildfire	Logging	Stress	Non-disturb.	Total
Confusion matrix, sample counts					
Wildfire	877	24	2	63	966
Logging	32	339	17	174	562
Stress	7	16	185	234	442
Non-dist. Forest	232	195	218	3385	4030
Total	1148	574	422	3856	6000
Confusion matrix, area proportion adjusted by mapped area proportion (see Table S4)					
Wildfire	0.00014	0.00000	0.00000	0.00001	0.00015
Logging	0.00008	0.00082	0.00004	0.00042	0.00136
Stress	0.00000	0.00000	0.00003	0.00003	0.00006
Non-dist. Forest	0.05748	0.04831	0.05401	0.83863	0.99843
Total	0.05769	0.04914	0.05408	0.83910	1.00000
OA	0.00014 + 0.00082 + 0.00003+ 0.83863 = 84.0%				

difficulties in distinguishing stress from other noisy factors such as phenological variation. Overall, disturbance agents that were detected earlier due to their stronger spectral separability (e.g., wildfire) tended to achieve higher mapping accuracy than those characterized by subtle spectral changes (e.g., stress).

Fig. 7 illustrates the site-specific lag–accuracy curves. Most curves exhibited an increasing trend with longer lags, as additional post-disturbance observations improved the extraction of trajectory-based features (e.g., slope and skewness) and the accumulation of consecutive anomalies helped suppress short-lived noise caused by phenological fluctuations. The curves generally plateaued at larger lag values, indicating that most disturbances had been detected by that stage. Fig. 7 also reveals pronounced regional differences in the performance of the proposed approach. For wildfire, the Xiangzhong Basin exhibited relatively lower UA, PA, and F_1 score compared with the other four sites, while its first-alert and level-off lags were of intermediate length. This may be attributed to its fragmented landscape and humid subtropical climate, both of which obscure distinct wildfire signals. For logging, the lowest accuracy occurred in Daxing'anling, likely due to small-scale selective harvesting and strong seasonal variability that complicate disturbance identification. For stress, the Yangtze Plain uniquely exhibited an inverted-U pattern, where accuracy initially increased but declined with longer observation windows, reflecting the rapid recovery of drought-induced spectral anomalies typical of this region. Overall, consistent with Fig. 6, both wildfire and logging exhibited shorter detection lags than stress, except in the Yunnan Plateau, where the confirmation lag was relatively longer (exceeding 20 days) for both wildfire and logging events.

4.2. Overall latency and accuracy

The mapped area proportions for wildfire, logging, stress, and non-

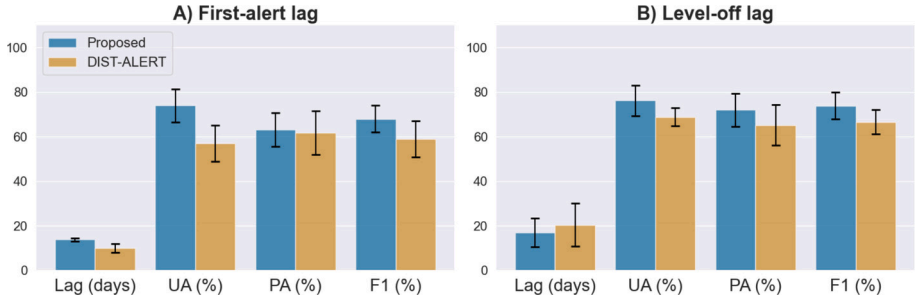

Fig. 8. The lag-accuracy curves and the accuracy metrics associated with two key lags for the binary maps produced by the proposed and DIST-ALERT for the five study sites.

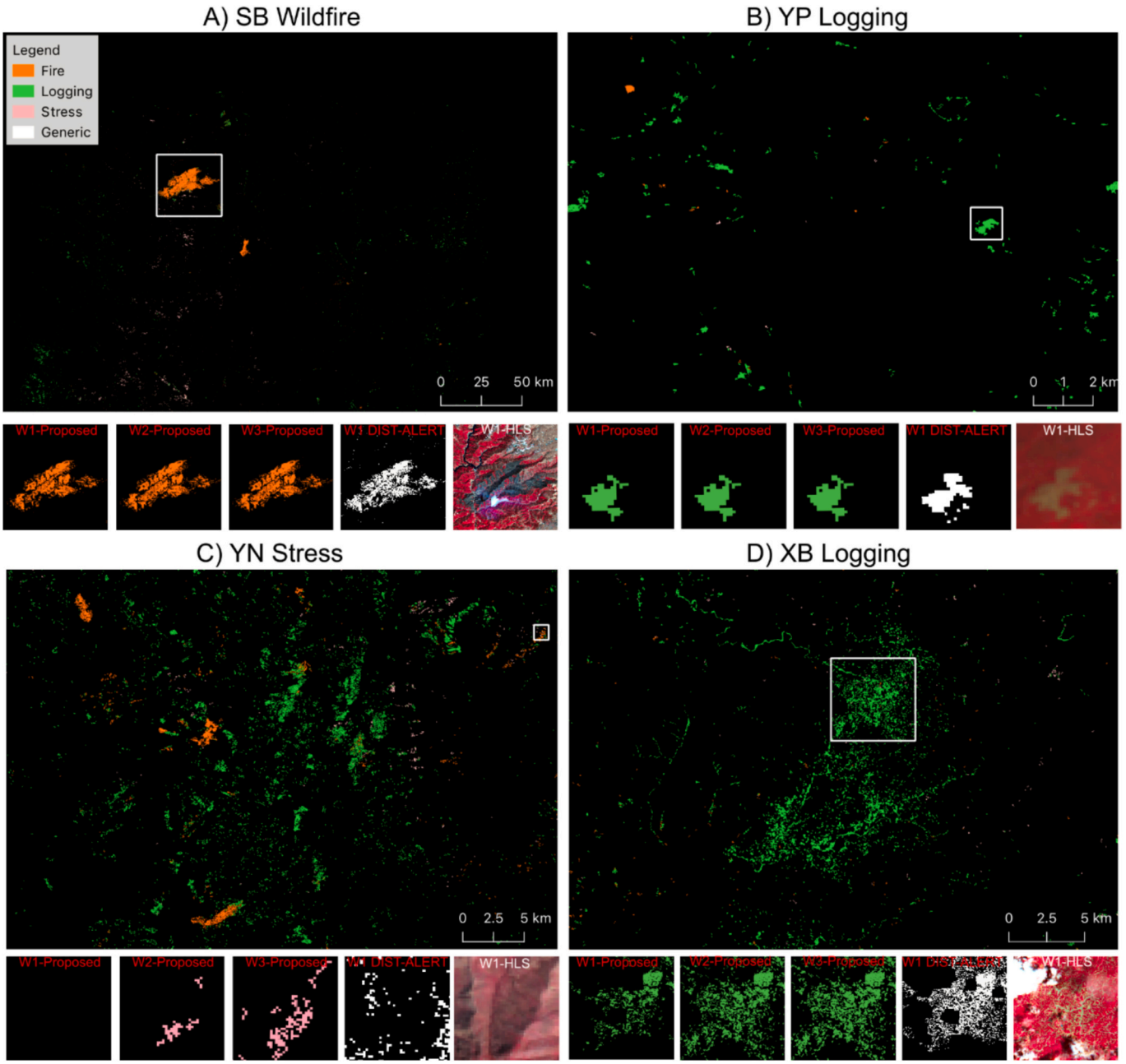

Fig. 9. Comparison between the proposed near-real-time (NRT) framework and the DIST-ALERT product across four representative study sites. The larger panels present the 2024 yearly ensemble maps in which only confirmed disturbance polygons (defined as those with an average number of consecutive anomalies >5) are retained. The smaller panels display weekly NRT results from the proposed framework for three consecutive weeks following disturbance onset (Weeks 1–3), alongside the corresponding DIST-ALERT binary disturbance maps and HLS image (NIR-Red-Green composite) for Week 1. (A) Sichuan Basin wildfire (29.8612° N, 101.5941° E); (B) Yangtze Plain logging (28.1069° N, 120.4240° E); (C) Yunnan Plateau stress disturbance (25.8580° N, 101.7880° E); (D) Xiangzhong Basin logging (26.0371° N, 113.5437° E). (For interpretation of the references to colour in this figure legend, the reader is referred to the web version of this article.)

disturbance forest were 0.00015, 0.00136, 0.00006, and 0.99843, respectively, calculated by aggregating the number of pixels assigned to each category across all weekly maps (see Table S4). Using these agent-specific mapped area proportions as weights, the overall first-alert and level-off lags were estimated to be 11.6 days and 15.5 days, respectively.

We further constructed confusion matrices for the two key lags (Tables 4 and 5) and estimated the overall accuracy by weighting agent-wise accuracy using the mapped area proportions. When the first alert was correctly triggered, the overall accuracy of the NRT map reached 77.5%. Once the performance plateau was achieved, the overall accuracy increased to 84.0%. This accuracy gain was mainly attributed to the reduction in commission errors for disturbance with the accumulation of consecutive observations, as the correctly labeled "non-disturbance" proportion increased from 0.763 to 0.834. It is worth noting that, for simplicity, we used a consistent set of mapped area proportions derived as the average across all weekly maps, although the true area proportions might vary with lag. For the site-based accuracy (Table S5 – S9 of the supplementary material), OA ranges from 68.5% (DX) to 83.2% (SB) for the first-alert lag, and from 81.5% (YP) to 86.6% (SB) for the level-off lag, which reflects that the accuracy for the level-off lag was more spatially robust than that for first-alert lag.

4.3. Comparison with DIST-ALERT

Fig. 8 compares the lag-accuracy curves of binary disturbance maps (disturbance vs. no-disturbance) generated by the proposed framework with those from the DIST-ALERT product. Site-specific lag-accuracy curves are provided in Fig. S6 of the supplementary material. The proposed approach shows a slightly longer first-alert lag than DIST-ALERT (13.8 days vs. 10.1 days) but achieves substantially higher user's accuracy (UA: 73.9% vs. 57.1%), leading to an improved F_1 score (0.680 vs. 0.590). For the level-off lag, the proposed framework demonstrates a shorter lag (17.0 vs. 20.4 days) and consistently higher accuracy metrics, including UA (76.1% vs. 68.8%), producer's accuracy (PA: 72.0% vs. 65.2%), and F_1 score (0.739 vs. 0.666). It should be noted that the lag metrics derived from the binary maps differ slightly from the overall lags reported in Section 4.2, which were calculated as weighted means across the three disturbance agents, reflecting differences in computational procedures. In addition, using snapshot-based confusion matrices adjusted by category area proportions at 21 lag days (when both methods had saturated accuracies, see Table S4 and S10), our approach still achieved a higher adjusted overall accuracy (86.26% vs. 81.74%, see Table S11 and S12 of the supplementary material). It is noteworthy that DIST-ALERT is an unsupervised system that does not require training-sample preparation, which improves operational flexibility but may partially explain its lower detection accuracy relative to our tile-calibrated, locally verified supervised framework.

Fig. 9 presents examples comparing the resultant disturbance maps generated by the proposed framework and the DIST-ALERT product. Overall, both approaches exhibit highly similar spatial patterns during the first week following the disturbance ("W1-proposed" and "W1 DIST-ALERT"), particularly for wildfire and logging due to their pronounced stand-removal signals. However, notable differences emerge for YN stress (Fig. 9C), where DIST-ALERT missed a considerable number of affected pixels. This discrepancy is likely attributable to differences in baseline estimation. Specifically, DIST-ALERT estimates baseline conditions using the minimum canopy loss observed within a $\pm$ 15-day temporal window over the preceding three years (Pickens et al., 2025), which may introduce uncertainties associated with phenological changes. In contrast, the CCDC-like approach compares each observation with its modeled baseline reflectance predicted precisely for the same calendar day, thereby minimizing seasonal bias. Additionally, DIST-ALERT tends to produce salt-and-pepper disturbance identification that are likely commission errors (see C) YN stress), whereas the proposed supervised framework integrates non-disturbance anomaly samples, effectively reducing false detections.

5. Discussion

5.1. Transferring-guided local samples

High-quality local samples are essential for accurately estimating category proportions and detecting region-specific disturbances. Ideally, these samples would be generated entirely from the study regions using local HLS time series. However, in regions where comprehensive historical disturbance products are scarce (e.g., much of China), building a representative training archive from scratch would require extensive manual interpretation over large areas and long time periods. A pragmatic alternative is to label only a small number of representative events, but this often leads to limited spatial and temporal coverage and can bias the training data toward a few disturbance episodes. To address this limitation, we propose a transferring-guided sample generation strategy that leverages abundant disturbance products available in CONUS to efficiently and consistently produce tile-specific local training datasets in China. Compared with the existing studies (e.g., Wang et al., 2025), which reported an interpretation rate of approximately 18 disturbance pixel samples per hour, our approach achieves a rate of ~850 sample patches per hour, yielding about 30,000 sample pixels in total. This substantial improvement in efficiency arises from transferring disturbance agent samples from CONUS to generate a preliminary disturbance patch map with accurately estimated anomaly dates, thereby minimizing the need for exhaustive manual delineation and temporal interpretation of historical disturbances. Interpreters were only required to record the sample IDs for which they had high confidence in the disturbance agent labels, based on time-series trajectories and three-year HLS imagery. Consequently, the transferring-guided strategy combines the temporal and spatial scalability of automated sample transfer with the accuracy of expert validation, enabling the production of high-quality, representative local samples at a fraction of the time and cost required by conventional manual annotation.

The verified patches are subsequently converted into pixel-based samples, ensuring sufficient sample numbers, and guaranteeing minimum representation even in regions where certain disturbance types are relatively rare. Benefiting from random and spatially even sampling across the region, the verified pixel samples not only provide a preliminary estimate of local cross-agent proportions but also support proportional allocation across disturbance categories, thereby improving the representativeness of training datasets and enhancing the performance of machine-learning models (Zhu et al., 2016). This design is particularly advantageous for large-scale monitoring tasks, where accurate class proportion and spatial distribution are critical for preventing model bias and ensuring robust generalization across different ecological and geographical contexts.

It is noteworthy that manual verification of the preliminary disturbance agent maps remains indispensable. We initially attempted to directly apply CONUS-based samples to train disturbance agent classification models for China. However, the resultant map quality proved unsatisfactory, even after strategically selecting the most representative CONUS samples based on vegetation and topographic similarity. As shown in Table S3 of the supplementary material, the high-confidence rates for wildfire and stress categories were both below 10%. This limitation likely arises from the large uncertainties embedded in post-disturbance spectral trajectories. Variations in forest management regimes, dominant vegetation species, and understory conditions between China and United States can substantially modify the temporal and spectral patterns following disturbances. Additionally, differences in climate regimes, disturbance intensity, and phenological cycles further exacerbate the mismatch, leading to reduced model transferability. These factors are inherently difficult to quantify and harmonize across regions at large spatial scales, making direct sample transfer insufficient for accurate classification. Consequently, manual verification is a critical safeguard to mitigate geographic bias by converting the transferred priors into locally valid training data, which ultimately improves the robustness of the final training dataset.

5.2. Latency

The lag time for mapping disturbance agents, influenced by both algorithmic and logistical factors, critically determines the effectiveness of an NRT monitoring system. In this study, we reported two key lag metrics, namely first-alert and level-off lag, to evaluate latency and model performance based on accuracy metrics at corresponding lag times. The first-alert lag, representing the average time required to produce a correct disturbance-agent classification, is particularly important for achieving rapid identification of disturbance type and extent. Although the NRT scenario was conducted under a weekly update scheme, the reported lag times in this study are still underestimated by approximately two days in an operational context, due to the actual delay in NASA's preprocessing of Landsat and Sentinel-2 imagery into HLS products.

In a standard CCDC workflow, monitoring typically relies on confirming a break and then re-initializing the model for the post-change segment, which can delay NRT alerts because break confirmation and re-initialization require multiple clear post-disturbance observations. In

contrast, our framework decouples anomaly detection from break confirmation and can issue disturbance alerts and agent attribution as soon as the first clear post-disturbance observation is available (i.e., $x = 1$). Break detection is applied conservatively only for persistent structural changes, preserving temporal continuity and reducing unnecessary resets during NRT operation. However, compared with our similar approach but for NRT binary disturbance mapping (Ye et al., 2024), the overall first-alert lag increased from 7.1 to 11.6 days under the same assumption of ignoring data latency. Two factors likely contributed to this increase. First, the previous evaluation was event-based (Ye et al., 2024), heavily influenced by several large disturbance events (e.g., Hurricane Ian and Mosquito Wildfire), whereas the validation in this study was time-uniformly sampled throughout the year rather than concentrated around major events. Second, the four-class agent classification task addressed here (wildfire, logging, stress, and non-disturbance) is inherently more complex than the binary disturbance detection problem, reducing the model's discriminative capacity during the early phase of disturbance development. For binary detection, our framework reported a longer first-alert lag than DIST-ALERT, reflecting a deliberate trade-off between timeliness and commission-error minimization achieved by our incorporating non-disturbance anomaly samples. The level-off lag represents the minimum lag time required to achieve stable and satisfactory performance. The overall level-off lag (15.5 days) was approximately four days longer than the first-alert lag, accompanied by a ~ 7% increase in OA. Given the weekly update scheme, these results indicate that our approach can identify most disturbance agents by the second week following disturbance onset (first-alert lag) and achieve a satisfactory overall map quality by the third week (level-off lag). These lag times could be further reduced by increasing the update frequency to daily, which, as reported by Ye et al. (2024), could shorten the detection lags by approximately five days. Such daily updates are particularly recommended for emergent events, where timeliness is given the highest operational priority.

Timeliness in an optical NRT monitoring system is also determined by the availability of clear observations, because a disturbance can only be detected after cloud free measurements are acquired. A recent global evaluation of HLS 2.0 cloud free coverage suggest that the mid latitude regions that include much of CONUS and our China study areas have broadly comparable clear observation densities (Zhou et al., 2025). This similarity supports the feasibility of transferring disturbance samples and applying an NRT framework originally developed and evaluated in CONUS to China (Ye et al., 2024). Nevertheless, seasonal and regional gaps in clear observations can still affect a CCDC-like algorithm by reducing valid observations available for model updating and by delaying the accumulation of consecutive anomalies. These effects can increase uncertainties in early-stage agent attribution and prolong detection lag. We note that future integration of complementary sensors, such as Sentinel-1 and GF-2, could further mitigate temporal gaps attributed to cloud.

5.3. Transferability to other regions

For regions whose vegetation and topography conditions are well represented in our CONUS archive, the sample-transfer step is expected to be more effective because the transferred samples provide a strong initialization for generating preliminary disturbance maps and efficiently guiding local verification. Transferability may be reduced in environments that differ substantially from CONUS, such as humid tropical regions, where persistent cloud cover and rapid vegetation recovery can alter spectral–temporal trajectories and weaken agent separability in optical data. In such cases, the workflow remains feasible, but it would likely require greater local verification effort and the incorporation of region-specific disturbance information (e.g., fire products, concession boundaries, or national inventories) to build a more representative initial sample pool. Moreover, incorporating management and social-economic datasets could further improve transfer performance for anthropogenic disturbances (such as logging) and enable expansion of the current disturbance feature set.

A second challenge in transferring to other regions is that locally dominant disturbance processes (e.g., shifting cultivation, selective logging, or mining) may require redefining the disturbance agent taxonomy. For example, we currently aggregated timber harvest, construction, and forest conversion into a single “logging” class because these canopy-removal processes often exhibit similar early-stage spectral responses in NRT optical observations. This aggregation can facilitate transfer to regions where fine-grained ancillary information is limited, but it may constrain management-oriented interpretation when more detailed attribution is needed. Future work will focus on developing a dynamic classification strategy that leverages longer post-disturbance observation windows to refine causal attribution and better differentiate disturbance agents across both similar and contrasting environments.

5.4. Stress disturbances

Stress-related disturbances typically produce subtle and spatially heterogeneous spectral responses, which makes NRT detection inherently more challenging than for abrupt stand-replacement events such as fire or logging. Nevertheless, even when change magnitudes are small, stress often exhibits a consistent spectral change direction (e.g., increases in SWIR2 associated with canopy moisture loss), suggesting that stress signals can still be detectable with a limited number of post-disturbance observations. In our results, the relatively low UA and PA for stress (both <60% at the level-off lag; Fig. 7) reflect this intrinsic difficulty and are further compounded by the lack of independent field datasets that can reliably define a precise onset date for gradual decline processes. However, stress is critically relevant for timely management responses (e.g., prioritizing follow-up inspections or initiating suppression in the case of pest outbreaks), especially given the increasing disturbance pressure under climate warming (Seidl et al., 2017). We therefore retained stress in the monitoring scope, but positioned it explicitly as an exploratory component aimed at providing early warning of canopy condition degradation. Future work will focus on improving robustness for this agent through integration of complementary data streams and constraints, such as climate anomalies, targeted field samples, and pest reports.

6. Conclusion

This study presents a novel NRT framework for mapping disturbance agents across China's forests using the Harmonized Landsat and Sentinel-2 (HLS) dataset. By integrating transferring-guided local sample generation, stage-based model construction, and anomaly-level detection, the proposed approach successfully identified major disturbance agents, i.e., wildfire, logging, and stress, within an average first-alert lag of approximately 12 days. The framework effectively overcomes the long-standing limitation of scarce local training data through an efficient transferring–guided strategy, which substantially reduced manual labeling efforts while maintaining high sample reliability. The stage-based models further enhanced the temporal sensitivity of agent classification, enabling early and accurate identification of disturbances with diverse spectral trajectories. Comparative assessments demonstrated that the approach achieved competitive latency and slightly better accuracy relative to existing global products while providing more actionable insights through disturbance-agent attribution. These findings highlight the feasibility of operationalizing fine-scale, NRT disturbance-agent monitoring across large regions and underscore the potential for extending the framework to other forested regions globally.

CRediT authorship contribution statement

Ronghua Liao: Writing – review & editing, Writing – original draft,

Visualization, Validation, Software, Methodology, Investigation, Formal analysis, Data curation, Conceptualization. **Chengcheng Guo:** Validation, Data curation. **Lingkun Chen:** Visualization, Validation, Data curation. **Yulin Jiang:** Validation, Data curation. **Yuchen Tao:** Visualization, Validation, Data curation. **Jiani Liao:** Data curation. **Rui Lu:** Validation, Data curation. **Huaguo Huang:** Visualization, Validation, Methodology, Conceptualization. **Zhou Shi:** Methodology, Conceptualization. **Su Ye:** Writing – original draft, Visualization, Writing – review & editing, Supervision, Methodology, Funding acquisition, Conceptualization.

Declaration of competing interest

The authors declare that they have no known competing financial interests or personal relationships that could have appeared to influence the work reported in this paper.

Acknowledgements

The authors are grateful for the financial support provided by National Key R&D Program of China (2024YFF1306200; 2024YFF1306201) and Fundamental and Interdisciplinary Disciplines Breakthrough Plan of the Ministry of Education of China (JYB2025XDXM909).

Appendix A. Supplementary data

Supplementary data to this article can be found online at https://doi.org/10.1016/j.rse.2026.115461.

Data availability

Data will be made available on request.

References

Andela, N., Morton, D.C., Schroeder, W., Chen, Y., Brando, P.M., Randerson, J.T., 2022. Tracking and classifying Amazon fire events in near real time. Sci. Adv. 8, eabd2713.

Baig, M.H.A., Zhang, L., Shuai, T., Tong, Q., 2014. Derivation of a tasselled cap transformation based on Landsat 8 at-satellite reflectance. Remote Sens. Lett. 5, 423–431.

Bullock, E.L., Healey, S.P., Yang, Z., Houborg, R., Gorelick, N., Tang, X., Andrianirina, C., 2022. Timeliness in forest change monitoring: a new assessment framework demonstrated using Sentinel-1 and a continuous change detection algorithm. Remote Sens. Environ. 276, 113043.

Cao, P., Zang, Z., Zhang, M., Wang, X., Tang, X., Xiang, J., Tang, S., Wang, J., Zhang, Y., 2025. Using LandTrendr to analyze forest disturbance, recovery, and attribution in Hunan province from 2001 to 2024. Ecol. Indic. 176, 113712.

Chen, Xi, Zhao, W., Chen, J., Qu, Y., Wu, D., Chen, Xuehong, 2021. Mapping large-scale forest disturbance types with multi-temporal CNN framework. Remote Sens. 13, 5177.

Cheng, K., Yang, H., Tao, S., Su, Y., Guan, H., Ren, Y., Hu, T., Li, W., Xu, G., Chen, M., 2024. Carbon storage through China's planted forest expansion. Nat. Commun. 15, 4106.

Claverie, M., Ju, J., Masek, J.G., Dungan, J.L., Vermote, E.F., Roger, J.-C., Skakun, S.V., Justice, C., 2018. The harmonized Landsat and Sentinel-2 surface reflectance data set. Remote Sens. Environ. 219, 145–161.

Cohen, W.B., Yang, Z., Stehman, S.V., Schroeder, T.A., Bell, D.M., Masek, J.G., Huang, C., Meigs, G.W., 2016. Forest disturbance across the conterminous United States from 1985–2012: the emerging dominance of forest decline. For. Ecol. Manag. 360, 242–252.

Cui, W., Yang, L., Zhang, L., Yang, C., Zhu, C., Zhou, C., 2025. A novel approach of generating pseudo revisited soil sample data based on environmental similarity for space-time soil organic carbon modelling. Int. J. Appl. Earth Obs. Geoinf. 139, 104542.

Dee, L.E., Miller, S.J., Helmstedt, K.J., Boersma, K.S., Polasky, S., Reich, P.B., 2025. Quantifying disturbance effects on ecosystem services in a changing climate. Nat. Ecol. Evol. 1–12.

Hansen, M.C., 2024. OPERA Land Surface Disturbance Annual from Harmonized Landsat Sentinel-2 Product (Version 1) [Data Set] [WWW Document]. NASA EOSDIS L. Process. Distrib. Act. Arch. Cent. https://doi.org/10.5067/SNWG/OPERA_L3_DIST-ANN-HLS_V1.001 (accessed 3.12.25).

Hansen, M.C., Krylov, A., Tyukavina, A., Potapov, P.V., Turubanova, S., Zutta, B., Ifo, S., Margono, B., Stolle, F., Moore, R., 2016. Humid tropical forest disturbance alerts using Landsat data. Environ. Res. Lett. 11, 34008.

Hawbaker, T.J., Vanderhoof, M.K., Schmidt, G.L., Beal, Y.-J., Picotte, J.J., Takacs, J.D., Falgout, J.T., Dwyer, J.L., 2020. The Landsat burned area algorithm and products for the conterminous United States. Remote Sens. Environ. 244, 111801.

Hermosilla, T., Wulder, M.A., White, J.C., Coops, N.C., Hobart, G.W., 2015. Regional detection, characterization, and attribution of annual forest change from 1984 to 2012 using Landsat-derived time-series metrics. Remote Sens. Environ. 170, 121–132.

Hermosilla, T., Wulder, M.A., White, J.C., Coops, N.C., Hobart, G.W., Campbell, L.B., 2016. Mass data processing of time series Landsat imagery: pixels to data products for forest monitoring. Int. J. Digit. Earth 9, 1035–1054.

Hou, G., Shen, X., Ge, S., Zhang, Y., Cao, L., 2025. A novel adaptive similarity-based ecological niche model for the endangered Yunnan snub-nosed monkey (*Rhinopithecus bieti*) using UAV LiDAR data. Remote Sens. Environ. 326, 114804.

Hu, T., Zhou, G., 2014. Drivers of lightning-and human-caused fire regimes in the great xing'an mountains. For. Ecol. Manag. 329, 49–58.

Johnson, E.W., Wittwer, D., 2008. Aerial detection surveys in the United States. Aust. For. 71, 212–215.

Ju, J., Zhou, Q., Freitag, B., Roy, D.P., Zhang, H.K., Sridhar, M., Mandel, J., Arab, S., Schmidt, G., Crawford, C.J., Gascon, F., Strobl, P.A., Masek, J.G., Neigh, C.S.R., 2025. The harmonized Landsat and Sentinel-2 version 2.0 surface reflectance dataset. Remote Sens. Environ. 324, 114723. https://doi.org/10.1016/j.rse.2025.114723.

Kennedy, R.E., Yang, Z., Braaten, J., Copass, C., Antonova, N., Jordan, C., Nelson, P., 2015. Attribution of disturbance change agent from Landsat time-series in support of habitat monitoring in the Puget Sound region, USA. Remote Sens. Environ. 166, 271–285.

Lin, Q., Huang, H., Chen, L., Wang, J., Huang, K., Liu, Y., 2021. Using the 3D model RAPID to invert the shoot dieback ratio of vertically heterogeneous Yunnan pine forests to detect beetle damage. Remote Sens. Environ. 260, 112475.

Oddo, P.C., Bolten, J.D., 2019. The value of near real-time earth observations for improved flood disaster response. Front. Environ. Sci. 7, 127.

Olofsson, P., Foody, G.M., Herold, M., Stehman, S.V., Woodcock, C.E., Wulder, M.A., 2014. Good practices for estimating area and assessing accuracy of land change. Remote Sens. Environ. 148, 42–57.

Olsson, P.-O., Lindström, J., Eklundh, L., 2016. Near real-time monitoring of insect induced defoliation in subalpine birch forests with MODIS derived NDVI. Remote Sens. Environ. 181, 42–53. https://doi.org/10.1016/j.rse.2016.03.040.

Pasquarella, V., Bradley, B., Woodcock, C., 2017. Near-real-time monitoring of insect defoliation using Landsat time series. Forests. https://doi.org/10.3390/f8080275.

Pastick, N.J., Jorgenson, M.T., Goetz, S.J., Jones, B.M., Wylie, B.K., Minsley, B.J., Genet, H., Knight, J.F., Swanson, D.K., Jorgenson, J.C., 2019. Spatiotemporal remote sensing of ecosystem change and causation across Alaska. Glob. Chang. Biol. 25, 1171–1189.

Perbet, P., Guindon, L., Côté, J.-F., Béland, M., 2024. Evaluating deep learning methods applied to Landsat time series subsequences to detect and classify boreal forest disturbances events: the challenge of partial and progressive disturbances. Remote Sens. Environ. 306, 114107.

Pickens, A.H., Hansen, M.C., Song, Z., Poulson, A., Komarova, A., Baggett, A., Kerr, T., Mikus, A., Ortiz Dominguez, C., Tyukavina, A., Lima, A., 2025. Rapid monitoring of global land change. Nat. Commun. 16, 8948. https://doi.org/10.1038/s41467-025-64014-9.

Qiu, S., Zhu, Z., Yang, X., Woodcock, C.E., Fahey, R.T., Stehman, S., Zhang, Y., Cullerton, M., Grinstead, A., Hong, F., Song, K., Suh, J.W., Li, T., Ren, W., Nemani, R. R., 2025. A shift from human-directed to undirected wild land disturbances in the USA. Nat. Geosci. 18, 989–996. https://doi.org/10.1038/s41561-025-01792-3.

Reiche, J., Hamunyela, E., Verbesselt, J., Hoekman, D., Herold, M., 2018. Improving near-real time deforestation monitoring in tropical dry forests by combining dense Sentinel-1 time series with Landsat and ALOS-2 PALSAR-2. Remote Sens. Environ. 204, 147–161.

Reymondin, L., Jarvis, A., Perez-Uribe, A., Touval, J., Argote, K., Rebetez, J., Guevara, E., Mulligan, M., 2012. Terra-I: A Methodology for near Real-Time Monitoring of Habitat Change at Continental Scales Using Modis-ndvi and trmm. CIAT-Terra-i.

Ryan, K.C., Opperman, T.S., 2013. LANDFIRE–A national vegetation/fuels data base for use in fuels treatment, restoration, and suppression planning. For. Ecol. Manag. 294, 208–216.

Sarre, A., 2020. Global forest resources assessment, 2020: Main report. Food and Agriculture Organization of the United Nations.

Schroeder, T.A., Schleeweis, K.G., Moisen, G.G., Toney, C., Cohen, W.B., Freeman, E.A., Yang, Z., Huang, C., 2017. Testing a Landsat-based approach for mapping disturbance causality in US forests. Remote Sens. Environ. 195, 230–243.

Seidl, R., Schelhaas, M.-J., Rammer, W., Verkerk, P.J., 2014. Increasing forest disturbances in Europe and their impact on carbon storage. Nat. Clim. Chang. 4, 806–810.

Seidl, R., Thom, D., Kautz, M., Martin-Benito, D., Peltoniemi, M., Vacchiano, G., Wild, J., Ascoli, D., Petr, M., Honkaniemi, J., 2017. Forest disturbances under climate change. Nat. Clim. Chang. 7, 395–402.

Shang, R., Zhu, Z., Zhang, J., Qiu, S., Yang, Z., Li, T., Yang, X., 2022. Near-real-time monitoring of land disturbance with harmonized Landsats 7–8 and Sentinel-2 data. Remote Sens. Environ. 278, 113073.

Shimizu, K., Ahmed, O.S., Ponce-Hernandez, R., Ota, T., Win, Z.C., Mizoue, N., Yoshida, S., 2017. Attribution of disturbance agents to forest change using a Landsat time series in tropical seasonal forests in the Bago Mountains, Myanmar. Forests 8, 218.

Silva, C.D.R., Olthoff, A.E., de la Mata, J.A.D., Alonso, A.P., 2013. Remote monitoring of forest insect defoliation. A review. For. Syst. 22, 377–391.

Slagter, B., Reiche, J., Marcos, D., Mullissa, A., Lossou, E., Peña-Claros, M., Herold, M., 2023. Monitoring direct drivers of small-scale tropical forest disturbance in near real-time with Sentinel-1 and-2 data. Remote Sens. Environ. 295, 113655.
Stahl, A.T., Andrus, R., Hicke, J.A., Hudak, A.T., Bright, B.C., Meddens, A.J.H., 2023. Automated attribution of forest disturbance types from remote sensing data: a synthesis. Remote Sens. Environ. 285, 113416.
Tang, X., Bullock, E.L., Olofsson, P., Estel, S., Woodcock, C.E., 2019. Near real-time monitoring of tropical forest disturbance: new algorithms and assessment framework. Remote Sens. Environ. 224, 202–218.
Tang, X., Bratley, K.H., Cho, K., Bullock, E.L., Olofsson, P., Woodcock, C.E., 2023. Near real-time monitoring of tropical forest disturbance by fusion of Landsat, Sentinel-2, and Sentinel-1 data. Remote Sens. Environ. 294, 113626.
Thom, D., Seidl, R., 2016. Natural disturbance impacts on ecosystem services and biodiversity in temperate and boreal forests. Biol. Rev. 91, 760–781.
Tyukavina, A., Hansen, M.C., Potapov, P.V., Stehman, S.V., Smith-Rodriguez, K., Okpa, C., Aguilar, R., 2017. Types and rates of forest disturbance in Brazilian legal Amazon, 2000–2013. Sci. Adv. 3, e1601047.
Verbesselt, J., Zeileis, A., Herold, M., 2012. Near real-time disturbance detection using satellite image time series. Remote Sens. Environ. 123, 98–108.
Verleysen, M., François, D., 2005. The curse of dimensionality in data mining and time series prediction. In: International Work-Conference on Artificial Neural Networks. Springer, pp. 758–770.
Wang, L., Liu, S., Song, W., Zhang, J., Ding, S., 2025. Global high-resolution forest disturbance type dataset. Earth Syst. Sci. Data Discuss. 2025, 1–23.
Wheeler, D., Hammer, D., Kraft, R., Steele, A., 2014. Satellite-Based Forest Clearing Detection in the Brazilian Amazon.
Woodcock, C.E., Allen, R., Anderson, M., Belward, A., Bindschadler, R., Cohen, W., Gao, F., Goward, S.N., Helder, D., Helmer, E., 2008. Free access to Landsat imagery. Science 320, 1011.
Wu, Z., He, H.S., Keane, R.E., Zhu, Z., Wang, Y., Shan, Y., 2019. Current and future patterns of forest fire occurrence in China. Int. J. Wildland Fire 29, 104–119.
Xian, G.Z., Smith, K., Wellington, D., Horton, J., Zhou, Q., Li, C., Auch, R., Brown, J.F., Zhu, Z., Reker, R.R., 2022. Implementation of the CCDC algorithm to produce the LCMAP collection 1.0 annual land surface change product. Earth Syst. Sci. Data 14, 143–162.
Xu, Q., Zhang, X., Li, J., Ren, J., Ren, L., Luo, Y., 2023. Pine wilt disease in northeast and Northwest China: a comprehensive risk review. Forests 14, 174.
Yang, J., Huang, X., 2021. 30 m annual land cover and its dynamics in China from 1990 to 2019. Earth Syst. Sci. Data Discuss. 2021, 1–29.
Yang, L., Meng, X., Zhang, X., 2011. SRTM DEM and its application advances. Int. J. Remote Sens. 32, 3875–3896.
Ye, S., Rogan, J., Zhu, Z., Eastman, J.R., 2021a. A near-real-time approach for monitoring forest disturbance using Landsat time series: stochastic continuous change detection. Remote Sens. Environ. https://doi.org/10.1016/j.rse.2020.112167.
Ye, S., Rogan, J., Zhu, Z., Hawbaker, T.J., Hart, S.J., Andrus, R.A., Meddens, A.J.H., Hicke, J.A., Eastman, J.R., Kulakowski, D., 2021b. Detecting subtle change from dense Landsat time series: case studies of mountain pine beetle and spruce beetle disturbance. Remote Sens. Environ. https://doi.org/10.1016/j.rse.2021.112560.
Ye, S., Zhu, Z., Suh, J.W., 2024. Leveraging past information and machine learning to accelerate land disturbance monitoring. Remote Sens. Environ. 305, 114071.
Zhang, Y., Woodcock, C.E., Chen, S., Wang, J.A., Sulla-Menashe, D., Zuo, Z., Olofsson, P., Wang, Y., Friedl, M.A., 2022. Mapping causal agents of disturbance in boreal and arctic ecosystems of North America using time series of Landsat data. Remote Sens. Environ. 272, 112935.
Zhang, B., Cai, D., Ai, S., Wang, H., Zuo, X., 2023. Research on the influencing factors and prevention measures of long-term forest fire risk in Northeast China. Ecol. Indic. 155, 110965.
Zhao, F., Liu, Y., Shu, L., 2020. Change in the fire season pattern from bimodal to unimodal under climate change: the case of Daxing'anling in Northeast China. Agric. For. Meteorol. 291, 108075.
Zhong, Z., He, B., Chen, Y., Yuan, W., Huang, L., Guo, L., Zhang, Y., Xie, X., 2021. Higher sensitivity of planted forests' productivity than natural forests to droughts in China. J. Geophys. Res. Biogeosci. 126, e2021JG006306.
Zhou, Q., Neigh, C.S.R., Ju, J., Dabney, P., Cook, B., Zhu, Z., Crawford, C.J., Gascon, F., Strobl, P., Sridhar, M., 2025. Towards seamless global 30-meter terrestrial monitoring: evaluating 2022 cloud free coverage of harmonized Landsat and Sentinel-2 (HLS) V2.0. IEEE Geosci. Remote Sens. Lett. 22, 1–5.
Zhu, Z., Woodcock, C.E., 2014. Continuous change detection and classification of land cover using all available Landsat data. Remote Sens. Environ. 144, 152–171.
Zhu, Z., Woodcock, C.E., Holden, C., Yang, Z., 2015. Generating synthetic Landsat images based on all available Landsat data: predicting Landsat surface reflectance at any given time. Remote Sens. Environ. 162, 67–83.
Zhu, Z., Gallant, A.L., Woodcock, C.E., Pengra, B., Olofsson, P., Loveland, T.R., Jin, S., Dahal, D., Yang, L., Auch, R.F., 2016. Optimizing selection of training and auxiliary data for operational land cover classification for the LCMAP initiative. ISPRS J. Photogramm. Remote Sens. 122, 206–221.
Zhu, A., Lu, G., Liu, J., Qin, C., Zhou, C., 2018. Spatial prediction based on third law of geography. Ann. GIS 24, 225–240.
Zhu, A.-X., Miao, Y., Liu, J., Bai, S., Zeng, C., Ma, T., Hong, H., 2019a. A similarity-based approach to sampling absence data for landslide susceptibility mapping using data-driven methods. Catena 183, 104188.
Zhu, Z., Zhang, J., Yang, Z., Aljaddani, A.H., Cohen, W.B., Qiu, S., Zhou, C., 2019b. Continuous monitoring of land disturbance based on Landsat time series. Remote Sens. Environ. https://doi.org/10.1016/j.rse.2019.03.009.
Zhu, Z., Zhang, J., Yang, Z., Aljaddani, A.H., Cohen, W.B., Qiu, S., Zhou, C., 2020. Continuous monitoring of land disturbance based on Landsat time series. Remote Sens. Environ. 238, 111116.
Zhu, Z., Qiu, S., Ye, S., 2022. Remote sensing of land change: a multifaceted perspective. Remote Sens. Environ. 282, 113266.